

EVALUATING DESIGN AND SAFETY OF ABDOMINAL AORTIC ANEURYSM
ENDOGRAFTS

A DISSERTATION

SUBMITTED TO THE DEPARTMENT OF MECHANICAL ENGINEERING
AND THE COMMITTEE ON GRADUATE STUDIES

OF STANFORD UNIVERSITY

IN PARTIAL FULFILLMENT OF THE REQUIREMENTS

FOR THE DEGREE OF

DOCTOR OF PHILOSOPHY

Polina A. Segalova

November 2011

Abstract

Abdominal aortic aneurysms (AAA's) are characterized by a permanent and irreversible enlargement of the abdominal aorta to at least 150 percent its expected normal size. Endovascular treatment of AAA's with endografts has gained tremendous popularity in the last decade, largely due to decreased perioperative mortality and faster recovery times, when compared to open surgical repair.

Although endografts are an appealing treatment option for many patients, some device design and safety issues have yet to be addressed. One of the biggest problems with endografts is their tendency to shift their position in the patient anatomy over time. The forces that cause this shift and their relation to endograft design are not well understood. In addition, the degree of blood damage due to the insertion of an endograft into the abdominal aorta has not been quantified. The following studies were completed in order to investigate the issues described above.

1. Calculation of endograft displacement force in patient-specific device models. This study used electron-beam computed tomography (CT) image data to generate patient-specific anatomical models using novel segmentation techniques. The patient models were then virtually modeled to represent three different endograft designs, based on aortic stent-graft devices already available in the U.S. or currently in clinical trials. Computational Fluid Dynamics (CFD) simulations were run to characterize the hemodynamic factors for each patient and a total displacement force was calculated for each model. Results show that the location of the device bifurcation impacts the overall displacement force, with proximal bifurcation endograft designs generating a lesser force than distal bifurcation designs.

2. Characterization of blood damage due to endograft placement. Patient-specific computational models were created to represent endograft features that partially obstruct blood flow to the renal arteries, which is sometimes necessary to attain complete exclusion of the aneurysm after deploying the device. Findings show that the insertion of an endograft causes a two-fold increase in blood damage. However, the magnitude of blood damage is within acceptable safety standards.

3. Benchtop testing of red blood cell damage. A benchtop experimental setup was created to measure the damage to red blood cells under various flow conditions and flow obstructions. Samples were characterized at different time points using light scatter methods to determine cell volume and hemoglobin concentration. Results indicate that significant damage to red blood cells occurs only after prolonged exposure ($>10^3$ seconds) to high shear (>4000 dynes/cm²) conditions. In addition, the presence of flow obstructions creates red blood cell fragments, instead of destroying the cells entirely.

Future directions for this work include additional CFD modeling of devices in more patients treated with different aortic stent graft designs to derive statistical significance relative to various design and anatomical features and extend the analysis to the evaluation of devices used for the treatment of thoracic aortic aneurysms (TAA's). Follow-up studies on device migration studies can also be completed in the cohort of patients where the endograft displacement forces were calculated. Further, blood damage models that incorporate the fragmentation of red blood cells can be developed.

Acknowledgements

Throughout my five years of graduate school at Stanford, I've been lucky enough to meet and work with many talented and supportive individuals. They've made it possible for me to complete my Ph.D., while growing both as a scholar and a person.

I would first like to thank my dissertation reading committee. Professor Sheri Sheppard and I initially met during my first year at Stanford, as I was attending a seminar on women in engineering. She's been an amazing force of guidance through my most challenging times as a graduate student. While always emphasizing the technical rigor of my work, she encouraged me to think beyond graduate school and explore various career paths. Professor Tom Kenny was the first person to welcome me to Stanford, when I visited the campus as a college senior. During my final year at Stanford, he played a key role in helping me finish my work and always had words of encouragement when something didn't go as expected. Professor Chris Zarins has been tremendously involved with my Ph.D. work, and his insight on the clinical implications of my findings has been invaluable. His timing for feedback is uncanny, as there have been numerous occasions when an encouraging email from Chris is just what I needed to get me to the next step. Finally, Dr. K.T. Rao has provided me with what few graduate students have: a true industry mentor. K.T. was always available to meet with me and give advice on how to make my work useful and relevant to the medical device industry. I was truly fortunate to leverage his years of experience working on medical devices for my Ph.D. work.

Several other individuals have helped me tremendously as I worked to complete my research. Professor Charley Taylor was the initial inspiration behind much of my

dissertation, and he is the person who first got me excited about medical devices through his teaching. Professor Stanley Schrier helped me in shaping the last part of my Ph.D. work. His feedback was always on point and I am incredibly grateful to him for taking the time to get to know my work and to chair my defense committee. He is also the person responsible for connecting me to Dr. Frans Kuypers at the Children's Hospital of Oakland Research Institute. Frans was kind enough to open his lab and his calendar to me, without which my work would not have been the same. I learned a tremendous amount working in Frans' lab, both as a researcher and as an engineer.

Members of the Taylor Lab at Stanford have provided me with everything from computer to moral support throughout my graduate studies. They are a group of incredibly caring, driven and thoughtful individuals. I would especially like to thank my collaborator Guanglei Xiong, who developed many of the segmentation methods used in my work. He's also been an incredible source of support and feedback during my writing process.

When not working on my Ph.D., I was fortunate enough to spend my time with friends who I know will stay with me for many years to come. Ashley, Alexia, Helen and Hanna have been the best roommates a grad student can ask for. Adela and Saniya have cheered me on as only a fellow mechanical engineer can. Paul, Emin, Joe, Genny, Nate, Megan, Paul, Megan, Dan, Archan, DJ, Amul, Josh and many others have helped me create some of my best memories at Stanford.

My family, especially my mom, deserve a special note of recognition. They've been unquestionably supportive and understanding throughout my graduate school years. My

mom is a constant inspiration and role model to me. Her strength and perseverance have shown me that anything is possible.

My fiancé, Matthew Colyer, has provided the foundation on which I was able to build my Ph.D. experience. He has been there as counselor, chef, computer expert, chauffer, mechanic, travel agent and general jack-of-all trades. He has carried me through my worst days and given me my happiest moments. His selfless support is something I will always be grateful for and will do my best to emulate as we start our lives as a married couple.

My dissertation work was supported by funds from the National Science Foundation Graduate Research Fellowship, Nellix Endovascular, and Endologix.

Table of Contents

1.	Introduction.....	1
1.1	Abdominal Aortic Aneurysms	1
1.2	Treatment of Abdominal Aortic Aneurysms	4
1.3	Computed Tomography	7
1.4	Computational Fluid Dynamics (CFD).....	9
1.4.1	Governing Equations for Incompressible Fluid Flow.....	9
1.4.2	Numerical Methods.....	11
1.4.3	Initial and Boundary Conditions.....	12
1.5	Numerical Simulations of Blood Flow	13
1.6	Thesis Overview	15
2	Evaluating Design of Abdominal Aortic Aneurysm Endografts in a Patient-Specific Model	17
2.1	Overview.....	17
2.2	Background.....	18
2.3	Methods.....	20
2.3.1	Patient Data.....	20
2.3.2	Model Construction	22
2.3.3	Boundary Conditions	24
2.3.4	Simulation.....	26
2.3.5	Displacement Force on Endograft	28
2.3.6	Curvature Analysis.....	29
2.3.7	Surface Area of Endograft	30

2.4	Results.....	30
2.4.1	Simulated Pressures and Flows.....	30
2.4.2	Displacement Force on Endograft	33
2.4.3	Endograft Curvature.....	37
2.4.4	Surface Area of Endograft	39
2.5	Discussion.....	42
2.5.1	Pressures and Flow	42
2.5.2	Displacement Force	43
2.5.3	Device Segments.....	45
2.5.4	Conclusion	46
2.5.5	Future Work	46
3	Computational Modeling of Shear-Based Hemolysis Due to Renal Obstruction....	47
3.1	Overview.....	47
3.2	Background.....	48
3.3	Methods.....	49
3.3.1	Patient Data.....	49
3.3.2	Model Construction	50
3.3.3	Boundary Conditions	52
3.3.4	Simulation.....	53
3.3.5	Reynolds Number	55
3.3.6	Stress Tensor and Scalar Stress.....	56
3.3.7	Normalized Index of Hemolysis	57
3.4	Results.....	58

3.4.1	Pressure and Volumetric Flow	58
3.4.2	Reynolds Number	59
3.4.3	Velocity.....	60
3.4.4	Stress.....	62
3.4.5	Normalized Index of Hemolysis	63
3.5	Discussion.....	64
3.5.1	Pressure and Flow	64
3.5.2	Reynolds Number	65
3.5.3	Velocity.....	65
3.5.4	Stress.....	65
3.5.5	Normalized Index of Hemolysis	66
3.5.6	Biological Factors	67
3.5.7	Conclusion	67
3.5.8	Future Work.....	68
4	Shear-Based Red Blood Cell Damage Due to Flow Obstruction	69
4.1	Overview.....	69
4.2	Background.....	70
4.3	Methods.....	71
4.3.1	Sample Preparation.....	71
4.3.2	Flow Circuit	72
4.3.3	Shear Stress Calculations.....	73
4.3.4	Advia 120 Hematology System	76
4.4	Results.....	78

4.4.1	Cell Counts.....	78
4.4.2	Cytograms.....	80
4.4.3	Light Microscopy Characterization	82
4.5	Discussion.....	83
4.5.1	Red Blood Cells.....	83
4.5.2	RBC Fragment Detection.....	84
4.5.3	Conclusion	86
4.5.4	Future Work.....	86
	References.....	88

List of Tables

Table 1.1. A list of FDA-approved EVAR devices is found above. All devices, with the exception of Guidant’s Ancure (*) are still found on the market.	7
Table 2.1. Summary of the patient anatomy and demographics, where BSA is the body surface area as calculated from the Mosteller formula in meters ² , HR is the patient’s heart rate in beats per minute, and BP is the blood pressure in millimeters of mercury.	21
Table 2.2. Summary of meshes generated for the Baseline model. A coarse mesh with a maximum element edge size of 1 mm and a fine mesh with a maximum element edge size of 0.5 mm were used.	26
Table 2.3. Summary of fine mesh data (with a maximum element edge size of 0.5mm) used in calculations for each of the four patient anatomies and their corresponding endograft models.	26
Table 2.4. Summary of target and simulated outlet flows for Patient 1.	31
Table 2.5. Summary of target and simulated outlet flows for Patient 2.	31
Table 2.6. Summary of target and simulated outlet flows for Patient 3.	32
Table 2.7. Summary of target and simulated outlet flows for Patient 4.	32
Table 2.8. Patient 1 displacement force.	35
Table 2.9. Patient 2 displacement force.	35
Table 2.10. Patient 3 displacement force.	36
Table 2.11. Patient 4 displacement force.	36
Table 2.12. Patient 1 curvature.	37
Table 2.13. Patient 2 curvature.	38
Table 2.14. Patient 3 curvature.	38

Table 2.15. Patient 4 curvature.....	38
Table 2.16. Patient 1 endograft surface area.....	40
Table 2.17. Patient 2 endograft surface area.....	40
Table 2.18. Patient 3 endograft surface area.....	41
Table 2.19. Patient 4 endograft surface area.....	41
Table 3.1. A demographic summary of the patients examined in this study, BSA is the body surface area in meters ² , HR is the heart rate in beats per minute and BP is the blood pressure in millimeters of mercury.....	49
Table 3.2. Total number of finite elements in each of the refined model meshes.....	54
Table 3.3. Computed Reynolds numbers for flow into the renal arteries, just distal to the renal ostia, for peak and average flow over the cardiac cycle.....	60
Table 3.4. Computed NIH values (g/100 L) for all six patient models.....	64
Table 3.5. ASTM standard F1841-97/F1830-97 classification of NIH levels and potential effects on clinical outcomes.....	66
Table 4.1. The above table summarizes the two types of flow used in the study and the resulting shear stress in the three different tube geometries.....	76

List of Figures

- Figure 1.1.** The above is an overview of the computational processes used throughout this work. The solid boxes depict the software modules, while the dashed boxes describe the files generated along each step..... 15
- Figure 2.1.** Volume renderings of the Baseline and Proximal Bifurcation CTA data sets used in this study are depicted. The Proximal Bifurcation device was anchored in the aneurysm sac with polymer, thus masking its double lumen design in the figure..... 21
- Figure 2.2.** The workflow for virtual intervention begins by isolating the aneurysm region and creating centerlines. The centerlines are then used to extend tubular endograft geometry and joined with a bifurcated section. 22
- Figure 2.3.** Four designs (Baseline, Proximal Bifurcation, Mid Bifurcation, and Distal bifurcation) were constructed for each of the four patient anatomies in this study and are pictured above. The three endograft geometries are highlighted in blue for each intervention model. 24
- Figure 2.4.** Pressure waveforms (solid, green line) at the inlet were calculated for each patient anatomy. The measured systolic (dashed, red line) and diastolic (dotted, blue line) patient blood pressures are also shown. There was no difference in the inlet blood pressure for a given patient anatomy across the four different models (Baseline, Proximal Bifurcation, Mid Bifurcation, and Distal Bifurcation). The maximums and minimums of the pressure waveform (solid, green line) were within 5% of the measured systolic (dashed, red line) and diastolic (dotted, blue line) blood pressure values, respectively... 33
- Figure 2.5.** The total curvature of each device design is plotted versus the total displacement force acting on each device. The three data points for each patient represent

the three device designs examined in this study. The correlation coefficient (R^2) is listed for each patient.....	39
Figure 2.6. The total endograft surface area (mm^2) in all three device designs is plotted versus the total force acting on the endograft. The correlation coefficient (R^2) is listed for each patient.	42
Figure 3.1. Maximum intensity projection (MIP) renderings of the CTA data sets used in this study for the three patients.	50
Figure 3.2. Geometric models were created for each patient based on CTA data using 2D segmentation techniques. In this method, centerlines were created along the desired vessels, which allowed for vessel segmentation. Finally, the vessel cross-sections were lofted together to generate the final geometric model.	51
Figure 3.3. Each patient Baseline model was altered to include a row of metal scaffold struts obstructing the renal ostia. The additional set of models is referred to as Endoframe models and is depicted above.	51
Figure 3.4. Pressure waveforms (green, solid line) at the inlet were computed for each patient anatomy. The measured systolic (red, dashed line) and diastolic (blue, dotted line) patient blood pressures are also displayed. There was no noteworthy difference in the inlet blood pressure between the Baseline and Endoframe models for a given patient. The pressure waveform maximums and minimums (green, solid line) were within 5% of the measured systolic (red, dashed line) and diastolic (blue, dotted line) blood pressure values, respectively.....	59

Figure 3.5. Volume rendering of the velocity magnitude (cm/s) in peak-systole for the Baseline and Endoframe models in all three patients. Velocities at a cross-section immediately distal to the renal artery ostia are also illustrated in a magnified view..... 61

Figure 3.6. Volume rendering of the scalar stress field of the Baseline and Endoframe models for Patients A - C. Stress field at a cross-sectional level immediately distal to the renal artery ostia is also illustrated in a magnified view. Elevated levels of stress can be seen around the endoframe struts for all Endoframe models..... 63

Figure 4.1. A schematic representation of the flow circuit is depicted in A., where three tubing segments of various diameter are connected in series and flow through the circuit is powered by a peristaltic pump. A photo of the flow circuit is shown in B..... 72

Figure 4.2. The ADVIA 120 Hematology system uses light scattered from a laser to analyze the cells present in a given sample. Low angle light scatter is measured to quantify the volume of a cell and high angle light scatter is used to describe the hemoglobin concentration present in a given sample. 77

Figure 4.3. A Volume/Hemoglobin Concentration cytogram generated by the ADVIA 120 using a normal RBC sample. Hemoglobin concentration in (g/dL) is plotted along the x-axis and the cell volume is plotted along the y-axis (fL)..... 78

Figure 4.4. Blood samples were analyzed in four different flow regimes using a combination of Low Flow (0.01 ml/s) and High Flow (0.1 ml/s) as well as a stainless steel mesh (wire diameter was 36 microns, distance between wires was 43 microns). Samples were analyzed for RBC concentration at five distinct time points..... 79

Figure 4.5. Four flow schemes were analyzed in this study incorporating Low Flow (0.01 ml/s) and High Flow (0.1 ml/s) with and without a stainless steel mesh (wire diameter

was 36 microns, distance between wires was 43 microns). The mean RBC fragment volume was recorded at five time points in each flow experiment.....	80
Figure 4.6. Cytograms for the Low Flow regime are pictured above at four time points: 10s, 100s, 1,000s and 10,000s. The composition of the sample remains largely unchanged, except for the last time point (10,000s) when some of the cells are detected outside the normal RBC volume and hemoglobin concentration.	81
Figure 4.7. Cytograms for the Hig Flow regime are pictured above at four time points: 10s, 100s, 1,000s and 10,000s. The samples undergo the most drastic change at the last time point, where almost no RBCs fall within the normal range of volume and hemoglobin concentration per cell.....	81
Figure 4.8. Samples from the Low Flow regime are seen at four different time points in the experiment.....	82
Figure 4.9. Samples from the High Flow regime are seen at four different time points in the experiment.....	83
Figure 4.10. The Volume/Hemoglobin Concentration cytogram is captured above for the four flow experiments at the final time point (10,000 seconds). The hemoglobin concentration is plotted along the x-axis and the volume is plotted along the y-axis. For normal RBC's, the majority of cells should fall in the central square.....	85
Figure 4.11. Light microscope image of RBCs during the last time point of all four flow regimes (Low Flow No Mesh, Low Flow Mesh, High Flow No Mesh, High Flow Mesh) examined in this study.	86

1. Introduction

1.1 *Abdominal Aortic Aneurysms*

Abdominal aortic aneurysms (AAA's) are characterized by a permanent and irreversible enlargement of the abdominal aorta to at least 150 percent its expected normal size. Aortic aneurysms occur most often in the infrarenal aorta, where a segment with a diameter greater than 3 cm is considered aneurismal [1]. The diameter of a healthy aorta varies with an individual's body weight, age, and sex. The vessel's diameter also gradually decreases as it advances from the thorax into the abdomen and finally the iliac bifurcation.

The disorder most often affects older males and is the 13th leading cause of death in the United States, resulting in over 15,000 deaths per year [2]. The incidence of AAA, estimated at 3-7 percent, has tripled over the last three decades [3]. As the U.S. population ages, the numbers of individuals affected by AAA's will continue to grow. Most AAA's are asymptomatic until rupture, although some patients report back discomfort or abdominal pain. Once ruptured, the aneurysm will be fatal in 65 percent of patients [4]. Patients undergoing surgical repair of AAA's are at risk for stroke, hemorrhage and other morbidities.

Although only 15 percent of AAAs eventually rupture, the risk of aneurysm rupture increases with aneurysm size [5]. In addition, the annual rate of growth on an abdominal aortic aneurysm increases with its size [6]. An aneurysm that reaches a diameter of 5 cm

is often an indication for intervention. At this size, the risk of rupture sees a steep increase and often outweighs the risk of intervention.

The underlying cause of AAA formation is the breakdown of the elastin and collagen structures in the tunica media layer of the abdominal aorta. This, in turn, leads to the destruction of medial smooth muscle cells (SMC's), which makes the aorta vulnerable to forces generated by its internal pressure. The elastin and collagen found in the vessel wall are primarily responsible for the mechanical properties of the abdominal aorta. This breakdown is, in turn, associated with inflammatory processes, neovascularisation, and creation of a range of proteases and cytokines [7-9]. Matrix metalloproteinase, or MMPs, are believed to play a crucial role in AAA formation. MMPs are derived from SMC's and macrophages. Specifically, increased levels of MMP-2, MMP-7, MMP-9, and MMP-12 are found in aneurismal tissue. It is believed that MMP-2 plays an important role in early aneurysm formation, as high levels of this constitutive enzyme are found in smaller AAA's. High levels of MMP-9 are found not only in aortic tissue but also in serum of AAA patients [4]. The proximal edge of AAAs exhibits high levels of MMP-12 and may be crucial in initiating AAA formation.

Inflammatory processes are believed to play an important role in AAA formation. As inflammatory cells migrate into the aortic wall, they release chemokines and cytokines, which cause further migration of leukocytes into the aortic wall. This causes the activation and expression of MMPs. These, in turn, cause the dilation of the aorta by destroying the medial layer of the vessels wall. As the vessel wall dilates, the stress experienced by the vessel causes further dilation and may eventually lead to rupture.

Although the exact cause of this chain reaction is not known, it is believed that genetic factors and atherosclerosis can influence the inflammatory process [10].

Hemodynamic factors, such as low wall shear stress, are believed to contribute to the progression and growths of AAA's [4]. Wall shear stress had been shown to affect inflammation, with the endothelial cells of vessels under low wall shear stress exhibiting a more round shape. This makes the endothelial layer more permeable to inflammatory cells. The infra-renal aorta is known to experience chronically low wall shear stress, partially due to the large flow to the kidneys, making it more vulnerable to AAA formation. The infra-renal aorta also sees an increase in pressure pulse magnitude due to wave reflection and aorta stiffening as the ratio of collagen to elastin is increased. Lower extremity vascular beds, which are more resistive, also contribute to AAA formation. This may be due to altered hemodynamics and increased pressure wave reflection. Therefore, patients with peripheral vascular occlusive disease, spinal cord injury and amputees are more likely to develop AAA's.

Overall, the vessel properties of AAA patients are drastically altered with the aorta becoming larger, stiffer and structurally weaker. The yield stress for an aneurismal aorta is lower when compared to a healthy vessel. The lamellar structure within the vessel wall is degraded and the thickness of the adventitia is increased. Aneurismal tissue is heterogeneous, which gives opportunity for focal stresses.

The balance of degradation and repair of collagen and elastin within the vessel wall shifts in aneurismal patients. The loss of elastin results in reduction of smooth muscle cells and transfers more of the load to collagen. As collagen fibers remodel under

increased load, the extracellular matrix experiences a creep causing the overall size of the aorta to increase.

Although some AAA's have specific causes, such as trauma or infection, the vast majority is associated with a variety of risk factors. Chronic smokers have been found to be four times more likely to develop AAA's than non-smokers [11, 12]. Genetic factors are also thought to be important, as the occurrence of AAA's in unrelated patients is only 1-3 percent but increases to 15-19 percent in first-degree relatives [13]. Genetic disorders, such as Marfan Syndrome and Ehlers Danlos Syndrome, predispose individuals to aneurysm formation. Males have been found to develop AAA more often than females [14, 15], who start to develop AAA's 10-15 years later than men. Advanced age is one risk factor for abdominal aortic aneurysms. AAA's begin to appear in persons aged 55 and are present in 10 percent of 80 year olds [16]. Atherosclerosis, hypertension and lower extremity disease are also considered risk factors [5, 17-19].

1.2 Treatment of Abdominal Aortic Aneurysms

There are three options open to patients diagnosed with AAA's: periodic monitoring, endovascular intervention, and surgery. The decision as to which option to follow is largely made by weighing the risk of rupture versus the risk of complications associated with treatment. The risk of rupture increases with the AAA diameter [20, 21], although smaller aneurysms have also been known to rupture [22, 23]. For smaller aneurysms (less than 4.5 cm), the risk of rupture is considered low and patients are imaged on an annual basis to monitor any changes in the aneurysm diameter. When the aorta becomes greater than 5.5 cm, surgery or endovascular intervention is recommended. At a diameter of 5.5

cm, the rupture rate is estimated at 11 percent and rises to 26 percent when the AAA reaches a diameter of 6.5 cm [24].

Surgical repair of AAA has long been the gold standard for treatment, but endovascular repair has been gaining broad acceptance since first being reported in 1991 [25, 26]. During a surgical repair of AAA's, the aorta is clamped and the patient is put on a heart-lung machine. The abdominal cavity is then opened and the aneurismal tissue is excised. In its place, a vascular graft is sutured. In contrast, EVAR introduces a device consisting of a metallic scaffold covered with fabric via catheter through a small incision in the femoral artery. The device is placed such that blood flow is excluded from the aneurysm sack and instead flows through the device lumen.

Endovascular aneurysm repair (EVAR) is associated with faster recovery times and a lower chance of mortality during the procedure, but it is not associated with higher survival rates two years after the procedure [1, 27]. An endoleak, defined as the presence of blood in the aneurysm sac after endovascular graft placement, is the most common complication linked to endograft usage. The leakage of blood into the aneurysm sac is thought to re-pressurize the sac and increase the risk of vessel rupture [28]. There are four types of endoleaks, as classified below:

Type I: Flow into the aneurysm sac due to an incomplete seal at the proximal or distal end of the endograft.

Type II: Flow into the aneurysm sac due to collateral vessels, such as the inferior mesenteric artery.

Type III: Flow into the aneurysm sac due to tears in the endograft material.

Type IV: Flow into the aneurysm sac due porosity of the endograft material.

A Type II endoleak is the most commonly occurring endoleak and the leading cause for re-intervention after device placement [29, 30].

Endografts have changed rapidly over the last 20 years. While there were only two devices approved by the U.S. Food and Drug Administration (FDA) in 1999, there are currently six FDA-approved EVAR devices sold in the U.S. (

Table 1.1). Over the years, these devices have shown improvements in fixation mechanisms, flexibility, durability, and ease of deployment. Although all currently approved endografts perform well when used in adherence to manufacturer's specifications and indicated use, problems arise when the devices are used in an "off-label" fashion. In addition, many patients who could potentially benefit from EVAR are not eligible for treatment due to exclusion criteria, such as a complex AAA anatomy [31]. The design challenge for the next generation of endografts is to overcome these limitations and eliminate many of these exclusion criteria.

Device Name	Manufacturer	FDA Approval Date
Ancure	Guidant Corporation	September 1999*
AneuRx	Medtronic, Inc., Minneapolis, MN	September 1999
Excluder	Gore & Associates, Flagstaff, AZ	November 2002
Zenith	Cook Medical, Bloomington, IN	May 2003
Powerlink	Endologix, Irvine, CA	October 2004
Talent	Medtronic, Inc., Minneapolis, MN	April 2008
Endurant	Medtronic, Inc., Minneapolis, MN	December 2010

Table 1.1. A list of FDA-approved EVAR devices. All devices, with the exception of Guidant's Ancure (*) are still found on the market.

1.3 Computed Tomography

Computed tomography (CT) utilizes x-rays to image the human body. A series of two-dimensional x-ray images are taken at a defined axis of rotation, creating a series of slices. Digital geometry processing is then used to reconstruct a three-dimensional volume of the subject's internal organs.

Each volumetric representation of the patient's anatomy is described by a series of slices. The thickness of the slices is variable and is determined by the operator. The x-rays are limited to passing through the slice thickness, minimizing scatter radiation. Each slice is further represented by pixels, and a matrix for each image is formed with the rows and columns of pixels. Using the thickness of each slice, the pixels are reconstructed into volumetric cubes, or voxels.

The anatomical structures in a CT image are rendered in varying shades of gray. The shade is determined by how much of the passing x-ray radiation is passed or

absorbed by a given tissue, which is determined by the density of the tissue. This is referred to as attenuation, and can be characterized by the following equation:

$$I = I_0 e^{-\mu x} \quad (0.1)$$

where I and I_0 are the recorded incident and transmitted x-ray intensities, μ is the attenuation coefficient, and x is the thickness of the anatomy. Water and muscle, for instance, have an attenuation coefficient of 1928 cm^{-1} and 1916 cm^{-1} , respectively. X-rays that travel through scanning volume unobstructed are recorded as black by the detectors, while x-rays that do not reach the detectors are represented as white areas on the final image. The rest of the image features a gradient of gray, which is determined by the density of a given tissue. The molecular structure determines the density of a tissue, with higher atomic numbers corresponding to denser tissues. For example, the lungs are rendered as mostly black on a CT image because they are filled with air, which is low density. On the other hand, any metallic implant present in the patient will show up as white.

Contrast agents are often used to highlight areas of the anatomy, which may otherwise not render on a CT scan. By filling the anatomy of interest with a high-density fluid, anatomical features, such as the contour of the abdominal aorta, can be easily recognizable. Iodine is often used as the contrast agent and is injected directly into the patient.

Hounsfield units (HUs), or CT numbers as they are sometimes called, quantify the degree to which x-rays are absorbed by a given material. Bone is represented as 1000 HUs, water is 0 HUs, and air is -1000 HUs. A wide spectrum of tissue can be

characterized by comparing the generated HUs to known material densities. For instance, blood and brain matter have a positive value, while fat will generate a negative HU value.

CT technology has progressed through several generations and recent advances in the field are allowing for greater image resolution and faster scan times. For instance, helical or spiral CT scanners involve the source and detector rotating about a predefined axis as the patient is moved at a constant rate along that axis. This technology reduces the x-ray dose for a given resolution and also diminishes the scan time.

CT rendering software has also seen tremendous advances in the last decade. It is possible to view CT data on reformatted planes, instead of just the standard axial, coronal and oblique views. Curved planar reformation allows for better visualization of curved structures, such as blood vessels. Volume rendering with color mapping is able to create vivid renderings of anatomical features.

1.4 Computational Fluid Dynamics (CFD)

1.4.1 Governing Equations for Incompressible Fluid Flow

Computational Fluid Dynamics (CFD) can be used to study the development and progression of cardiovascular disease [32, 33]. CFD uses numerical methods to solve the Navier-Stokes equations, Eq. (0.2), which describe conservation of momentum. When coupled with the principle of conservation of mass, Eq. (0.3), and appropriate boundary and initial conditions, an arbitrary finite element mesh can be used to compute the pressure and velocity over the given domain.

$$\rho \left(\frac{\partial \bar{u}}{\partial t} + \bar{u} \cdot \nabla \bar{u} \right) = -\nabla P + \mu \nabla^2 \bar{u} \quad (0.2)$$

$$\nabla \cdot \bar{u} = 0 \quad (0.3)$$

In the above equations, ρ is the fluid density, \bar{u} is the velocity, P is the pressure and μ is the dynamic viscosity of the fluid. The first term in Eq. (0.2), $\rho \frac{\partial \bar{u}}{\partial t}$, represents the blood acceleration. The next term, $\rho \bar{u} \cdot \nabla \bar{u}$, calculates the blood advection. On the right hand side of Eq. (0.2), $-\nabla P$ is the pressure gradient experienced by the flow and $\mu \nabla^2 \bar{u}$ are the viscous forces. Several important assumptions can be made about the blood flow in large vessels, such as the abdominal aorta. Blood can be modeled as a viscous, incompressible Newtonian fluid. In reality, blood is a suspension of red blood cells, white blood cells and platelets in plasma and exhibits non-Newtonian behavior, so that its viscosity changes depending on the shear rate experienced by the flow. However, these behaviors only become relevant in small blood vessels, such as capillaries, where the diameter of the arteries becomes comparable to the cell size. Since blood plasma is mostly water, incompressible flow has been considered a good model for blood. Finally, any gravitational forces acting on the blood flow are considered negligible.

The computational domain for a given simulation can be derived directly from patient image data, such as CT scans. A finite element mesh based on that geometry can be generated to the user's specification. Patient information, such as heart rate and blood pressure, can also be incorporated into the simulation process. The ability to extract patient-specific geometry coupled with patient-specific boundary conditions is a powerful tool for understanding and selecting the best treatment option for a given patient [33].

CFD models also have the potential to play an important role in the development of medical devices. Animal studies and benchtop models are two ways new medical devices are currently tested for durability, efficacy and safety. Although both of these methods can answer key questions about a given device design, they can be expensive and time-consuming to implement. In addition, it can be difficult to isolate and assess specific parameters while prescribing all test conditions. Computational modeling provides the opportunity to fully define a testing scenario and has the potential to deliver targeted answers on shorter time scales. CFD also allows for the study of blood flow at higher resolutions than is possible to measure with benchtop or animal models.

1.4.2 Numerical Methods

The equations described in the previous section can be solved using several methods: Finite Difference, Finite Element, and Finite Volume Methods. The Finite Difference Method relies replacing the system of partial differential equations with a finite difference scheme, thus generating a system of algebraic equations. These equations are then solved. In the Finite Element Method, the domain in question is divided into a number of small, simple elements and a set of algebraic equations is used to represent a certain quantity (such as fluid velocity) based on a given force and fluid viscosity. The quantity in question is interpolated by a polynomial over a given element. Since connecting elements share nodes, the quantity is interpolated over the entire computational domain in a piecewise fashion. The Finite Volume Method is similar to the above two methods in that it uses a system of algebraic equations to calculate a certain value at discrete places on a geometric mesh. In this method, volume integrals in the

formulating equations are converted to surface integrals and the divergence theorem is used to compute a solution. All these methods are numerical techniques for finding an approximate solution to the equations for a specific point in time. Finite Element based methods were used to study blood flow in this work.

1.4.3 Initial and Boundary Conditions

The proper use of initial and boundary conditions in a given simulation is crucial to ensure that a meaningful solution is generated. Since the modeling domain does not encompass the entirety of the patient's vasculature, boundary conditions are needed to define what happens outside the model domain at the vessel boundaries. Boundary conditions play an important role in determining the flow distribution to each vessel outlet. At the inlet of the model, an inflow waveform is prescribed. The amount of flow entering an inlet can be determined from magnetic resonance imaging (MRI) scans or prescribed based on literature. The determined mean flow rate is mapped onto a velocity profile at the inlet of the model. Every simulation described in this work is initialized by providing an inflow waveform at the inlet surface of each simulation domain.

The boundary conditions specify the effects downstream vasculature on the computational domain. Specifically, they determine the level of pressure as well as the flow splits between that various blood vessels in the model. Several methods exist for boundary condition formulation. Impedance and resistance boundary conditions two types of outlet boundary conditions used in flow simulations. Impedance boundary conditions are modeled as,

$$Z(\omega) = \frac{P(\omega)}{Q(\omega)} \quad (0.4)$$

where Z is the impedance, ω is the frequency, P is the pressure and Q is the volumetric flow. As ω approaches zero, flow becomes steady.

Resistance boundary models draw an analogy between current flow through a resistor and blood flow through an artery, such that:

$$P = QR \quad (0.5)$$

In order to represent a compliant vessel, the above relationship can be altered by using the Windkessel or RCR model. The Windkessel model uses a proximal resistance, R_p , a capacitance, C , and a distal resistance, R_d . Resistance boundary conditions are relatively simple to implement, allows for physiological levels of pressure, and provides the user with control over the flow splits. However, these types of boundary conditions also amplify the pressure pulse, damp the flow pulse and force the flow and pressure to be in phase. The simulations described in this paper utilize resistance boundary conditions.

1.5 Numerical Simulations of Blood Flow

The numerical simulation work described in this document was completed using the SimVascular software developed at Stanford University under the supervision of Professor Charles Taylor. Three-dimensional blood flow simulations over a user-defined domain are generated by solving the three-dimensional Navier-Stokes equations. The user-defined domains featured in this work are extracted directly from patient CT data sets. SimVascular was developed from PHASTA (Parallel, Hierarchical, Adaptive,

Stabilized, Transient Analysis), an academic finite element code, and uses the Stabilized Finite Element theory pioneered by Professor Thomas J.R. Hughes [34].

The PHASTA software can model several flow regimes, including:

- Laminar and turbulent flow
- Steady and unsteady flow
- Compressible and incompressible flow

The software is a compilation of over 100 scripts written in Fortran 90 and C++ and has several features, which lend themselves well to efficient flow simulations. The code uses Message Passing Interface (MPI) so that simulations can be run on numerous processors. A regular desktop can be used to complete simple simulations, but the code is easily scalable for more complex jobs. The majority of simulations described in this work were completed using Stanford's Bio-X² computer cluster, which features 20.6 teraflops and a total of 2,208 cores. The PHASTA code also allows for different polynomial orders to be assigned over the finite element mesh, although this work only uses linear tetrahedral elements. The size of the finite elements is adaptive, giving the user the ability to generate highly anisotropic meshes. This feature was used extensively in the work described in Chapter 3, allowing for a better numerical solution while keeping the overall mesh size manageable. Equal-order interpolating functions were used for the velocity and pressure fields. This is known as the SUPG (Streamline-Upwind Petrov-Galerkin) formulation. SUPG also allows for numerical stability in both the diffusive and advective limits.

Several steps are required in order to create and launch a flow simulation with SimVascular. The process starts out with solid model creation, which is extracted from

patient image data. The solid model is then discretized into finite elements, and files describing the mesh are passed to the pre-solver of SimVascular. The code utilizes the mesh and the given initial and boundary conditions along with the geometric description of the domain. The SimVascular pre-solver generates a set of files, which is ready to be passed to the main solver to run the blood flow analysis. The simulation is then ready to be run, which is usually done over at least five cardiac cycles to ensure that the simulation stabilizes. The generated numerical solution describes the pressure and velocity over the finite element mesh over specific time points. Visualization files can then be generated to analyze the hemodynamic effects represented by the numerical solution. Open source software, such as ParaView, can be used to generate visualizations of the solution. An overview of the entire process is illustrated in Figure 1.1.

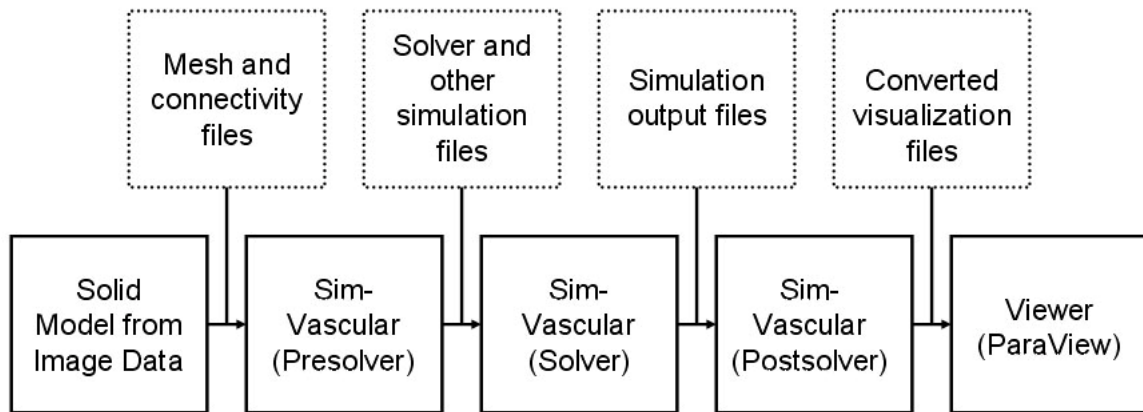


Figure 1.1. Overview of the computational processes used throughout this work. The solid boxes depict the software modules, while the dashed boxes describe the files generated along each step.

1.6 Thesis Overview

The goal of this work is to address some of the frequently asked questions about abdominal aortic endograft design and safety. Graft migration is one of the biggest issues facing AAA endografts, and so Chapter 2 evaluated the overall displacement force experienced by endografts of various designs. Once displacement forces are more

understood, it will be possible to design better devices that experience less displacement over time. Along with displacement forces, blood damage is also a concern in patients treated with endografts, especially when endograft elements obstruct blood flow. Chapter 3 describes a computational study that quantifies the damage to red blood cells caused by the presence of an implantable device in the abdominal aorta. Finally, Chapter 4 provides benchtop experimental results for shear-based blood damage, based on the results found in Chapter 3. Future directions for research include characterizing forces on devices for thoracic aortic aneurysms (TAA's) and creating better models for blood damage.

2 Evaluating Design of Abdominal Aortic Aneurysm Endografts in a Patient-Specific Model

2.1 Overview

Computer modeling of blood flow in patient-specific anatomies can be a powerful tool for evaluating the design of implantable medical devices. Three different endograft designs, which are commonly used to treat patients with abdominal aortic aneurysms, were assessed. Once implanted, the endograft may shift within the patient's aorta allowing blood to flow into the aneurismal sac. One potential cause for this movement is the pulsatile force experienced by the endograft over the cardiac cycle.

We used contrast-enhanced computed tomography angiography (CTA) data from four patients with diagnosed AAAs to build patient-specific models using 3D segmentation. For each of the four patients, baseline model from the patient's pre-operative CTA data was constructed. In addition, geometries characterizing three distinct endograft designs were created, differing by where each device bifurcated into two limbs (Proximal Bifurcation, Mid Bifurcation and Distal Bifurcation). Computational fluid dynamics was used to simulate blood flow, utilizing patient-specific boundary conditions. Pressures, flows and displacement forces on the endograft surface were calculated. The curvature and surface area of each device was quantified for all patients.

The magnitude of the total displacement force on each device ranged from 2.43 N to 8.68 N for the four patients examined. Within each of the four patient anatomies, the total displacement force was similar (varying at least by 0.12 N and at most by 1.43 N),

although there were some differences in the direction of component forces. Proximal Bifurcation and Distal Bifurcation geometries consistently generated the smallest and largest displacement forces, respectively, with forces observed in the Mid Bifurcation design falling in between the two devices. The smallest curvature corresponded to the smallest total displacement force and higher curvature values generally corresponded to higher magnitudes of displacement force. The same trend was seen for the surface area of each device, with lower surface areas resulting in lower displacement forces and vice versa. The patient with the highest blood pressure displayed the highest magnitudes of displacement force.

The data indicate that curvature, device surface area and patient blood pressure impact the magnitude of displacement force acting on the device. Endograft design may influence the displacement force experienced by an implanted endograft, with the Proximal Bifurcation design showing a small advantage for minimizing the displacement force on endografts.

2.2 Background

Design and evaluation of implantable medical devices often relies on benchtop testing using physical models and animal laboratory studies. Although both methods are needed, they can be costly to implement and unable to represent patient-specific physiological conditions. Computer simulations of blood flow in patient-specific anatomies offer an attractive option to supplement these existing testing methods in order to further evaluate implantable devices, such as stent grafts used to treat aneurysms of the abdominal aorta [33].

Abdominal aortic aneurysms (AAAs) are the 13th leading cause of death for males in the U.S. [2, 35], with endovascular aneurysm repair (EVAR) becoming a popular alternative to traditional, open surgical repair [10, 36]. Although EVAR offers faster recovery times and the ability to treat patients who may otherwise not be eligible for open repair, endografts may shift in position over time, which can result in additional interventions, conversions to open repair or even death [37, 38]. The shift in endograft position is attributed to the pulsatile nature of blood flow and the resulting forces [39].

There are several FDA-approved endografts currently available in the U.S. market. One of the key features of each endograft's geometry is the location at which its body bifurcates into two limbs, which then extend into the iliac arteries. Some devices place the bifurcation point closer to the renal arteries, while other devices maintain a single lumen until splitting at the aortic bifurcation. In this study, CFD was used to evaluate three device designs in patient-specific models built using 3D segmentation techniques. The first model (Proximal Bifurcation) featured an entirely double lumen design. The second model (Mid Bifurcation) was created with a bifurcation point mid-way between the renal arteries and the aortic bifurcation. The last model (Distal Bifurcation) divided into its two limbs at the aortic bifurcation. The displacement forces on the surface of all three device designs were calculated to compare which device would experience the most force.

2.3 Methods

2.3.1 Patient Data

For the purpose of this study, imaging data was selected from four male patients with diagnosed AAAs and average age 59.5 years (SD: 6.56; range: 54-69) from a previously-acquired and anonymized database. The patients' medical overview can be found in Table 2.1. The patients had varying morphologies of AAA (Angulated – Patient 1, Fusiform – Patient 2, Iliac – Patient 3, and No neck – Patient 4), in order to represent the different types of anatomies that can be treated with an endograft. An aneurysm with an Angulated neck presents a special challenge for positioning and fixation of most AAA endografts, while a Fusiform anatomy describes a uniform bulging of the abdominal aorta. An Iliac anatomy refers to an AAA, which also has involvement of one or both of the iliac arteries. Finally, a No Neck anatomy refers to an aneurysm with no or little (less than 1 cm) healthy tissue distal to the renal arteries, where most AAA endografts are fixated.

Each of the four patients examined in this study was treated with a novel AAA endograft, featuring an entirely double lumen design (Proximal Bifurcation). Before undergoing the procedure, each patient's age, sex, mass, height, heart rate, systolic blood pressure, and diastolic blood pressure were recorded (Table 2.1). All four patients presented with abdominal pulsation upon pre-operative examination. Further, Patients 3 and 4, had a history of smoking. Patient 3 had a history of diabetes and stenosis of both superficial femoral arteries. Patient 4 had undergone a coronary artery bypass graft five years before undergoing the EVAR procedure. Baseline and 30 day follow up scans,

using contrast-enhanced computed tomography angiography (CTA), were obtained from each patient, as seen in Figure 2.1

Patient	AAA Morph.	Age	Sex	Mass (kg)	Height (m)	Mosteller BSA (m ²)	HR (bpm)	Sys. BP (mm Hg)	Dias. BP (mm Hg)
1	Angulated	69	M	67	1.70	1.78	70	150	100
2	Fusiform	54	M	72	1.95	1.97	107	135	70
3	Iliac	57	M	75	1.68	1.87	95	140	70
4	No Neck	58	M	72	1.80	1.90	53	140	70

Table 2.1. Summary of the patient anatomy and demographics, where BSA is the body surface area as calculated from the Mosteller formula in meters², HR is the patient's heart rate in beats per minute, and BP is the blood pressure in millimeters of mercury.

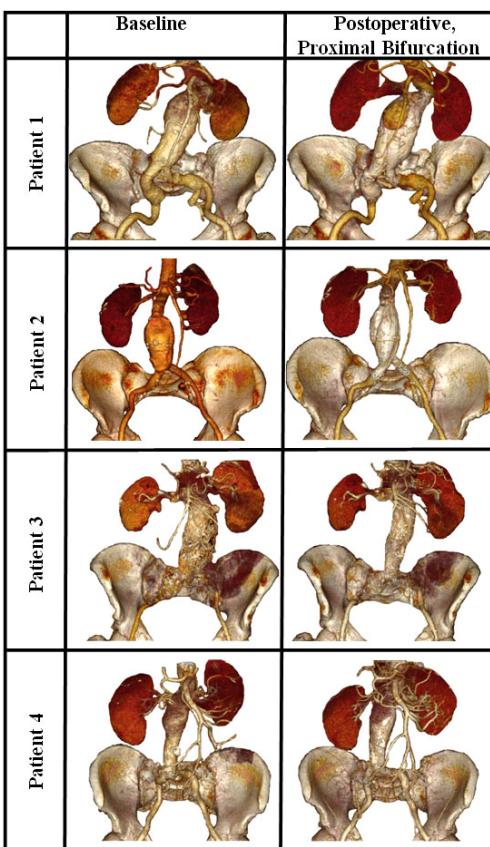


Figure 2.1. Volume renderings of the Baseline and Proximal Bifurcation CTA data sets used in this study. The Proximal Bifurcation device was anchored in the aneurysm sac with polymer, thus masking its double lumen design in the figure.

2.3.2 Model Construction

The abdominal aorta for each patient in this study was segmented using itk-SNAP [40]. The 3D segmentation capabilities of this software provide some advantages over the traditional 2D segmentation approach [41, 42], in which a series of 2D segmentation is performed on a vessel's cross section along the centerline of that vessel. In addition to being more time efficient, 3D segmentation is less subjective and better able to capture detailed patient anatomy. The segmentations derived from itk-SNAP were edited further using custom software [43] by trimming vessel outlets and then used to generate volumetric finite element meshes. In addition to the abdominal aorta, the following nine arteries were included in each model: hepatic, splenic, superior mesenteric, left renal, right renal, left external iliac, right external iliac, left internal iliac and right internal iliac.

Two of the four patient geometries were created (Baseline and Proximal Bifurcation designs) directly from the acquired CTA image data from patients. The remaining two device designs (Mid Bifurcation and Distal Bifurcation designs) were created by performing virtual intervention on the Baseline model, using methods developed by Xiong, et. al. [44] and illustrated in Figure 2.2.

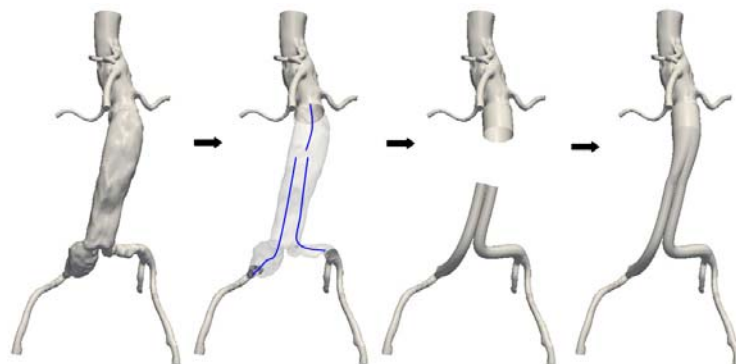


Figure 2.2. The workflow for virtual intervention begins by isolating the aneurysm region and creating centerlines. The centerlines are then used to extend tubular endograft geometry and joined with a bifurcated section.

The process began by excluding the entire length of the aneurysm, including a portion of the iliac arteries. Centerlines to guide the virtually implanted device limbs and body were then generated and an endograft defined by those centerlines was created. The radius of the proximal end of the endograft was prescribed to match the radius of the aorta at that location. Similarly, the radii of the distal endograft ends were constructed to match the radii of their respective right and left common iliac arteries. The bifurcation point in the Mid Bifurcation model was chosen half-way between the proximal end of the endograft and the aortic bifurcation. In the Distal Bifurcation model, the endograft split into two lumens at the aortic bifurcation. Figure 2.3 illustrates the four computational domains constructed for this study, with black representing the three different types of endograft evaluated.

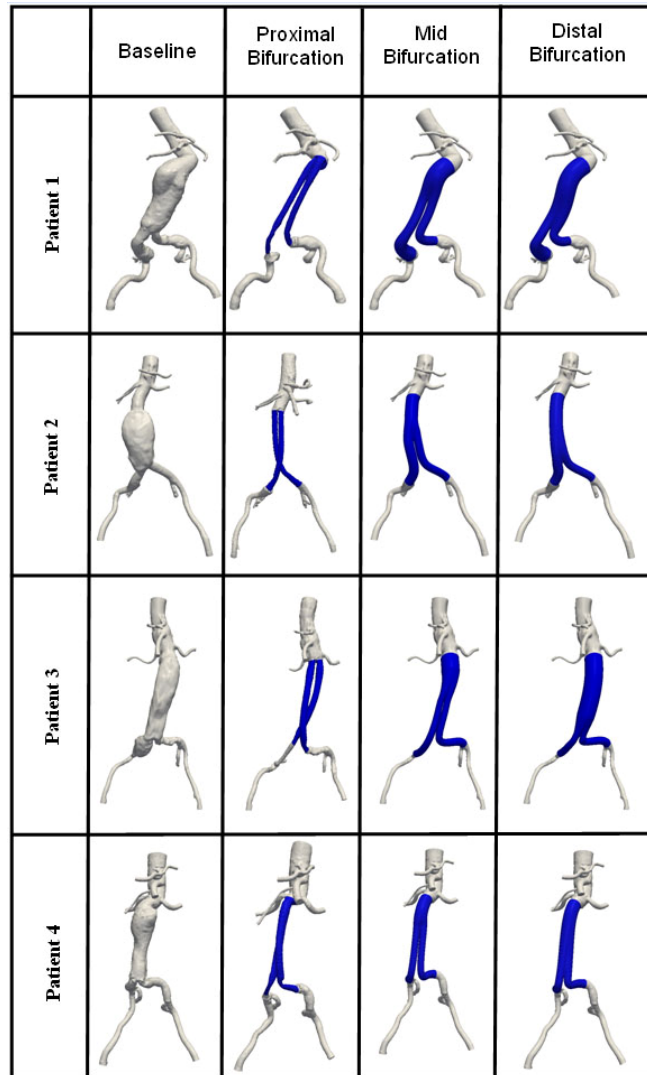


Figure 2.3. Four designs (Baseline, Proximal Bifurcation, Mid Bifurcation, and Distal bifurcation) were constructed for each of the four patient anatomies in this study and are pictured above. The three endograft geometries are highlighted in blue for each intervention model.

2.3.3 Boundary Conditions

A volumetric inflow waveform was prescribed at the inlet of each model based on a Phase-Contrast Magnetic Resonance Imaging (PC-MRI) population study completed by Les, et. al. [4] and described by Eq. (2.1) and Eq. (2.2). The waveform was adjusted in accordance with the morphometric parameters described in the population study using

each patient's calculated body surface areas (BSA) according to the Mosteller formula, Eq. (2.3).

$$SCFlow_{mean} = 16.4(BSA)^{1.56} \quad (2.1)$$

$$IRFlow_{mean} = 3.98(BSA)^{2.00} \quad (2.2)$$

$$BSA = \sqrt{\frac{Height \times Weight}{36}} \quad (2.3)$$

Equations (2.1) and (2.2) describe the patient's mean supraceliac (*SCFlow*) and infrarenal volumetric (*IRFlow*) blood flows, respectively, as a function of the body surface area. The mean volumetric flows are calculated in milliliters per second (ml/s), the BSA used is in square meters (m²), the height is in meters (m) and the weight is in kilograms (kg).

The impedance of the downstream vasculature was represented at each outlet with a three-element Windkessel or RCR model. The three components of the model, R_p , C , and R_d , represent the resistance of the proximal arteries, the artery compliance and the distal resistance of the vascular bed, respectively. The values of the RCR parameters were initially calculated based on the patient's average blood pressure over the cardiac cycle, flow splits from literature [4], total resistance and total compliance. The RCR parameters were tuned during the Baseline model simulation to coincide with the patient's pressure and expected flow splits. This simulation was originally run and tuned on a coarse isotropic mesh for each of the four Baseline patient models with a maximum edge size of 1 mm, Table 2.2. A finer isotropic mesh was then generated for all sixteen models, Table 2.3. The same RCR parameter values tuned on the Baseline models were then applied to each of the three endograft model simulations.

BASELINE	Coarse Mesh (1mm)	Fine Mesh (0.5 mm)
<i>Patient 1</i>	4,661,627	14,845,760
<i>Patient 2</i>	3,058,329	9,811,155
<i>Patient 3</i>	3,186,671	10,175,486
<i>Patient 4</i>	2,781,679	8,639,885
Average	3,422,077	10,868,072
St. Dev.	843,470	2,731,518

Table 2.2. Summary of meshes generated for the Baseline model. A coarse mesh with a maximum element edge size of 1 mm and a fine mesh with a maximum element edge size of 0.5 mm were used.

FINE MESH	Proximal Bifurcation	Mid Bifurcation	Distal Bifurcation
<i>Patient 1</i>	7,944,102	10,193,144	10,897,008
<i>Patient 2</i>	4,942,770	5,990,896	6,000,818
<i>Patient 3</i>	5,732,706	7,145,479	8,540,243
<i>Patient 4</i>	6,163,228	6,212,200	6,448,265
Average	6,195,702	7,385,430	7,971,584
St. Dev.	1,270,454	1,937,527	2,242,461

Table 2.3. Summary of fine mesh data (with a maximum element edge size of 0.5mm) used in calculations for each of the four patient anatomies and their corresponding endograft models.

2.3.4 Simulation

Each Baseline model was first discretized into a coarse isotropic finite-element volume mesh using a commercial meshing kernel (MeshSimTM, Simmetrix, Troy, NY) with linear tetrahedral elements having a maximum edge size of 1 mm. The average number of elements was 3,422,077 (SD: 843,470; range: 2,781,679-4,661,627), as summarized in Table 2.2.

We ran steady simulations with the predicted inflow based on patient body surface area and resistance outlet boundary conditions based on the patient's measured blood pressure and expected flow splits. Once the desired pressures and flow conditions were achieved, the results were used to run a pulsatile simulation. This time, RCR outlet boundary conditions were utilized and adjusted such that the calculated pressure at the

model inflow was within 5 percent of the patient's measured systolic and diastolic blood pressure. The flow to each outlet was also ensured to be within 5 percent of the expected volumetric flow. This was accomplished by tuning the various parameters in the RCR boundary conditions. In general, increasing the capacitance (C) resulted in a smaller pulse pressure (and vice versa) and increasing the total resistance (R) increased the blood pressure. It should be noted that the majority of the resistance at each vessel outlet is due to the downstream vasculature, representing the capillary bed. As such, 94.4 percent of the resistance was prescribed to R_{distal} , with the remaining amount going to R_{proximal} . The noted exception is the renal arteries, which were assigned R_{distal} value 72 percent of R_{total} to account for the relatively low resistance of the kidneys' vascular bed. The boundary conditions of the pulsatile simulation were tuned until the desired inlet pressure and outlet flow was achieved. The last step in this process was to create a final isotropic mesh with a maximum edge size of 0.5 mm. For the Baseline models, this resulted in meshes that had an average of 10,868,071 elements (SD: 2,731,518; range: 8,639,885-14,845,760), Table 2.2.

We calculated the pressure and velocity fields by solving the incompressible Navier-Stokes equations with a custom stabilized finite-element solver. The viscosity ($\mu=0.04$ P) and density ($\rho=1.06$ g/cm³) of blood were assumed to be constant and gravity was neglected. The walls of the models were set to be rigid and a no-slip velocity condition was prescribed at the walls. The shape of the velocity profile was constrained at each outlet with an augmented Lagrangian method [39] to avoid divergence during retrograde flow. It is important to note that this method does not affect the overall amount of flow leaving each outlet, it simply constrains the shape. The simulation for each model was

run for eight cardiac cycles, to ensure convergence and an acceptably low residual or error. A time step of $1/1000^{\text{th}}$ of the cardiac cycle was used for each simulation with up to eight non-linear iterations per time step. The same boundary conditions determined during the Baseline model simulations for the four patients were then applied to each set of three device models. Table 2.2 and Table 2.3 summarize the final mesh sizes used in this study.

2.3.5 Displacement Force on Endograft

We calculated the displacement force exerted on each of the three endograft designs in Patients 1-4 by integrating all the traction components acting on each device surface. Thus, the total displacement force affecting each endograft is a function of the pressure and shear stress acting on the device. The calculated force was further divided into anterior, lateral and axial displacement forces. To explore the difference between the three device designs, the force acting on each device left limb, right limb and body was computed. The left and right device limbs are defined as the surfaces distal to the point of bifurcation, extending into the left and right iliac arteries, respectively. The body of the device is defined as the surface starting at the proximal end of the endograft and terminating at the bifurcation point. For the Proximal Bifurcation design, the force acting on the body was computed as the force exerted on the shelf created at the proximal device end. As with the total displacement force calculation, the forces acting on each device component (right limb, left limb and body) were also reported as components in the anterior, lateral and axial directions.

$$\vec{F} = \int_A \vec{T} dA \quad (2.4)$$

$$\vec{T} = PA\vec{n} + \vec{\tau} \quad (2.5)$$

where \vec{F} is the total force exerted, \vec{T} is the traction, A is the area, P is the pressure, \vec{n} is the surface normal, and $\vec{\tau}$ is the wall shear stress.

2.3.6 Curvature Analysis

We calculated the magnitude of curvature for each device based on the centerlines associated with its components. That is, each of the Mid Bifurcation and Distal Bifurcation device models had three centerlines each to represent the body, left and right limbs of the devices. The Proximal Bifurcation geometries, on the other hand, only had two centerlines each, representing their left and right limbs, since their body component is effectively a shelf created when the double-lumen device meets the single lumen abdominal aorta. Once the curvatures for all components for a given device were calculated, a weighted average based on the length of each centerline was taken to determine the total device curvature.

For the purpose of this study, curvature magnitude was defined as the rate at which the unit tangent to the curve rotates, as characterized by Eq. (2.6),

$$\kappa = \left\| \frac{d\mathbf{T}}{ds} \right\| \quad (2.6)$$

where κ is the curvature magnitude in mm^{-1} , \mathbf{T} is the unit tangent to the curve, and s is the curve being described. For a straight line, the unit tangent would experience no rotation and the curvature would therefore be zero. In contrast, a tight curve would require the unit tangent to rotate quickly and would thus generate a high curvature value. Another

way to define the curvature is to inscribe a circle along the curve in question that most closely represent it at the given location. The inverse of that circle's radius will be the local curvature of that curve and the units of curvature are consequently length^{-1} . The centerline of each device was defined using 1,000 points and calculated the curvature along each centerline.

2.3.7 Surface Area of Endograft

The surface area of the twelve devices in this study was calculated. The total surface area for each device as well as its components (right limb, left limb and body) were quantified. In the case of the Proximal Bifurcation device design, the body component refers to the shelf created on the proximal end of the device, as the single lumen aorta meets the double-lumen device.

2.4 Results

2.4.1 Simulated Pressures and Flows

The CFD pressure recorded at the Baseline model's inflow face agreed well with the patient's measured systolic and diastolic pressures, as can be seen in

Figure 2.4. Patient 1 had the highest systolic and diastolic blood pressures, and Patient 2 had the largest deviation (4.2 mmHg) from the target pressure.

Volumetric Flow for Patient 1	Target (ml/s)	Baseline Model (ml/s)	Proximal Bifurcation Model (ml/s)	Mid Bifurcation Model (ml/s)	Distal Bifurcation Model (ml/s)
<i>Hepatic</i>	4.6	4.6	4.6	4.6	4.6
<i>Splenic</i>	4.6	4.6	4.7	4.6	4.6
<i>SMA</i>	6.2	6.4	6.4	6.4	6.4
<i>Left Renal</i>	6.2	6.3	6.3	6.3	6.3
<i>Right Renal</i>	6.2	6.2	6.3	6.1	6.1
<i>Left External Iliac</i>	4.5	4.4	4.3	4.4	4.4
<i>Right External Iliac</i>	4.5	4.4	4.3	4.4	4.4
<i>Left Internal Iliac</i>	1.9	1.9	1.9	1.9	1.9
<i>Right Internal Iliac</i>	1.9	1.9	1.9	1.9	1.9

Table 2.4. Summary of target and simulated outlet flows for Patient 1.

The volumetric flow recorded at each outlet also agreed well with the target flows, as seen in Table 2.4 - Table 2.7 for the Baseline models. As expected, the majority of flow goes to the renal arteries. The hepatic and splenic arteries also received considerable flow.

Volumetric Flow for Patient 2	Target (ml/s)	Baseline Model (ml/s)	Proximal Bifurcation Model (ml/s)	Mid Bifurcation Model (ml/s)	Distal Bifurcation Model (ml/s)
<i>Hepatic</i>	5.2	5.3	5.3	5.2	5.3
<i>Splenic</i>	5.2	5.3	5.3	5.3	5.3
<i>SMA</i>	7.1	7.2	7.2	7.2	7.2
<i>Left Renal</i>	7.1	7.2	7.2	7.2	7.2
<i>Right Renal</i>	4.3	4.4	4.4	4.4	4.4
<i>Right Renal Accessory</i>	2.8	2.9	2.8	2.8	2.8
<i>Left External Iliac</i>	5.4	5.2	5.2	5.2	5.1
<i>Right External Iliac</i>	5.4	5.2	5.2	5.2	5.2
<i>Left Internal Iliac</i>	2.3	2.3	2.3	2.3	2.3
<i>Right Internal Iliac</i>	2.3	2.3	2.3	2.3	2.3

Table 2.5. Summary of target and simulated outlet flows for Patient 2.

Volumetric Flow for Patient 3	Target (ml/s)	Baseline Model (ml/s)	Proximal Bifurcation Model (ml/s)	Mid Bifurcation Model (ml/s)	Distal Bifurcation Model (ml/s)
<i>Hepatic</i>	4.9	4.9	4.5	4.8	4.6
<i>Splenic</i>	4.9	4.8	4.9	5.0	4.9
<i>SMA</i>	6.6	6.8	6.9	6.7	7.0
<i>Left Renal</i>	6.6	6.7	6.7	6.7	6.8
<i>Right Renal</i>	6.6	6.4	6.3	5.9	5.8
<i>Left External Iliac</i>	4.9	4.9	4.9	5.0	5.0
<i>Right External Iliac</i>	4.9	4.8	5.0	5.0	2.2
<i>Left Internal Iliac</i>	2.1	2.1	2.1	2.1	5.0
<i>Right Internal Iliac</i>	2.1	2.1	2.1	2.2	2.2

Table 2.6. Summary of target and simulated outlet flows for Patient 3.

Volumetric Flow for Patient 4	Target (ml/s)	Baseline Model (ml/s)	Proximal Bifurcation Model (ml/s)	Mid Bifurcation Model (ml/s)	Distal Bifurcation Model (ml/s)
<i>Hepatic</i>	5.0	5.1	5.1	5.0	5.0
<i>Splenic</i>	5.0	5.1	5.0	4.9	4.9
<i>SMA</i>	6.8	6.9	7.0	6.9	6.9
<i>Left Renal</i>	6.8	6.9	6.9	6.9	6.9
<i>Right Renal</i>	5.1	5.1	5.2	5.2	5.2
<i>Right Renal Accessory</i>	1.7	1.7	1.7	1.7	1.7
<i>Left External Iliac</i>	5.0	5.2	4.8	4.9	4.9
<i>Right External Iliac</i>	5.0	5.2	4.8	4.9	4.9
<i>Left Internal Iliac</i>	2.2	2.2	2.1	2.1	2.1
<i>Right Internal Iliac</i>	2.2	2.2	2.0	2.1	2.1

Table 2.7. Summary of target and simulated outlet flows for Patient 4.

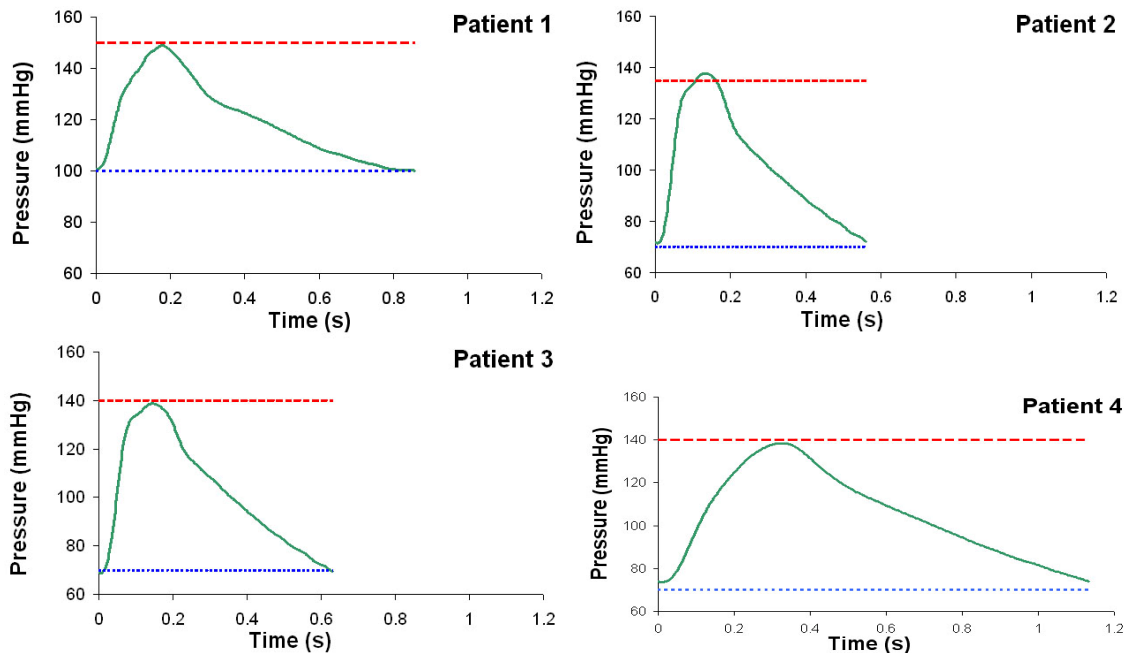


Figure 2.4. Pressure waveforms (solid, green line) at the inlet were calculated for each patient anatomy. The measured systolic (dashed, red line) and diastolic (dotted, blue line) patient blood pressures are also shown. There was no difference in the inlet blood pressure for a given patient anatomy across the four different models (Baseline, Proximal Bifurcation, Mid Bifurcation, and Distal Bifurcation). The maximums and minimums of the pressure waveform (solid, green line) were within 5% of the measured systolic (dashed, red line) and diastolic (dotted, blue line) blood pressure values, respectively.

2.4.2 Displacement Force on Endograft

We calculated the average displacement force over one cardiac cycle for all three device models and the findings are reported in Figure 2.4. The total average displacement force across all patients varied from a minimum of 2.43 N (in Patient 2's Proximal Bifurcation model) to a maximum of 8.68 N (in Patient 1's Distal Bifurcation model). The range of forces across the three device designs was 1.43 N, 0.54 N, 0.12 N and 0.62 N for Patients 1-4, respectively. The total displacement force for each patient was smallest for the Proximal Bifurcation design, largest for the Distal Bifurcation and between the two for Mid Bifurcation.

The displacement force acting on the body segment of the device only was 0.78 N, 0.83 N, 1.91 N, and 1.96N for Patients 1-4, respectively. The force acting exclusively on the device body was smallest in the Distal Bifurcation model for all patients, except Patient 2. In addition, the lateral and axial components were almost always negative (thus, pointing in the right and caudal directions, respectively) with the only exception of a positive axial component in the Distal Bifurcation model of Patient 2. Similarly, the anterior components of the force acting on the device body are mostly positive (thus pointing to the front of the body), except for the negative anterior components in the Proximal Bifurcation model of Patient 3.

The displacement force ranges calculated in the right limb segment of the devices across the four patients are 2.21 N, 0.70 N, 0.24 N, and 2.32 N for Patients 1-4, respectively. The forces acting on the right limb of the device only are always greatest in the Distal Bifurcation model. More axial and lateral components are negative than not (implying a force that more often points to the right and dorsal directions) and vice versa for the anterior component (implying a force that often points to the front of the body).

Patient 1		Proximal Bifurcation	Mid Bifurcation	Distal Bifurcation
Displacement Force, Total	Magnitude	7.25	7.88	8.68
	<i>Anterior</i>	4.41	5.41	5.71
	<i>Lateral</i>	-4.00	-5.58	-6.35
	<i>Axial</i>	-4.14	-1.31	-1.55
Displacement Force, Body	Magnitude	2.90	2.61	2.12
	<i>Anterior</i>	1.57	1.84	1.24
	<i>Lateral</i>	-0.96	-1.72	-1.72
	<i>Axial</i>	-2.24	-0.68	-0.15
Displacement Force, Right Limb	Magnitude	1.50	2.49	3.71
	<i>Anterior</i>	1.03	2.05	3.06
	<i>Lateral</i>	-0.62	-1.40	-2.10
	<i>Axial</i>	-0.90	0.20	0.12
Displacement Force, Left Limb	Magnitude	3.18	3.00	3.28
	<i>Anterior</i>	1.81	1.51	1.42
	<i>Lateral</i>	-2.42	-2.46	-2.53
	<i>Axial</i>	-1.00	-0.84	-1.52

Table 2.8. Patient 1 displacement force.

Patient 2		Proximal Bifurcation	Mid Bifurcation	Distal Bifurcation
Displacement Force, Total	Magnitude	2.43	2.72	2.97
	<i>Anterior</i>	1.95	2.31	2.83
	<i>Lateral</i>	-0.95	-1.32	0.33
	<i>Axial</i>	-1.10	-0.56	-0.82
Displacement Force, Body	Magnitude	0.87	0.97	1.70
	<i>Anterior</i>	0.59	0.88	1.69
	<i>Lateral</i>	-0.29	-0.33	-0.08
	<i>Axial</i>	-0.57	-0.24	0.13
Displacement Force, Right Limb	Magnitude	0.61	0.80	1.31
	<i>Anterior</i>	0.53	0.76	0.82
	<i>Lateral</i>	-0.12	-0.20	0.88
	<i>Axial</i>	-0.28	-0.12	-0.51
Displacement Force, Left Limb	Magnitude	1.03	1.06	0.72
	<i>Anterior</i>	0.84	0.67	0.32
	<i>Lateral</i>	-0.54	-0.79	-0.46
	<i>Axial</i>	-0.25	-0.21	-0.44

Table 2.9. Patient 2 displacement force.

Patient 3		Proximal Bifurcation	Mid Bifurcation	Distal Bifurcation
Displacement Force, Total	Magnitude	4.33	4.41	4.45
	<i>Anterior</i>	-0.35	1.52	1.64
	<i>Lateral</i>	-0.25	-0.43	-0.55
	<i>Axial</i>	-4.31	-4.12	-4.10
Displacement Force, Body	Magnitude	2.24	1.83	0.33
	<i>Anterior</i>	-0.11	0.58	0.23
	<i>Lateral</i>	-0.08	-0.11	-0.13
	<i>Axial</i>	-2.24	-1.73	-0.21
Displacement Force, Right Limb	Magnitude	1.08	1.00	1.24
	<i>Anterior</i>	-0.09	0.50	0.90
	<i>Lateral</i>	-0.03	-0.06	-0.21
	<i>Axial</i>	-1.08	-0.87	-0.82
Displacement Force, Left Limb	Magnitude	1.01	1.61	3.12
	<i>Anterior</i>	-0.15	0.44	0.51
	<i>Lateral</i>	-0.14	-0.26	-0.21
	<i>Axial</i>	-0.99	-1.52	-3.08

Table 2.10. Patient 3 displacement force.

Patient 4		Proximal Bifurcation	Mid Bifurcation	Distal Bifurcation
Displacement Force, Total	Magnitude	5.93	6.39	6.55
	<i>Anterior</i>	4.50	5.44	4.94
	<i>Lateral</i>	-2.20	-1.53	-2.18
	<i>Axial</i>	-3.17	-2.99	-3.71
Displacement Force, Body	Magnitude	2.03	2.58	0.56
	<i>Anterior</i>	1.13	2.36	0.35
	<i>Lateral</i>	-0.77	-0.30	-0.44
	<i>Axial</i>	-1.50	-0.99	-0.06
Displacement Force, Right Limb	Magnitude	1.66	1.96	3.34
	<i>Anterior</i>	1.36	1.78	2.80
	<i>Lateral</i>	-0.25	0.14	-0.51
	<i>Axial</i>	-0.92	-0.82	-1.75
Displacement Force, Left Limb	Magnitude	2.44	2.23	2.89
	<i>Anterior</i>	2.01	1.30	1.79
	<i>Lateral</i>	-1.18	-1.36	-1.24
	<i>Axial</i>	-0.75	-1.19	-1.90

Table 2.11. Patient 4 displacement force.

Table 2.8-2.11. The displacement force, in Newtons, was calculated over surface of each of the three device models. The above table lists the magnitude of the migration force as well as its components. The forces acting on the individual limbs and main body of the device are also reported. In the case of the Proximal Bifurcation geometry, the Body segment of the device refers to the shelf created at the proximal end of the device.

The ranges of displacement force for the left limb device segment are 0.28 N, 0.34 N, 2.11 N, and 1.18 N for Patients 1-4, respectively. With the exception of Patient 2, the greatest displacement force is exerted in the Distal Bifurcation model. For the left limb, the lateral and axial components are all negative, which translates to a force acting in the

right and dorsal directions. In addition, all the anterior components, except in the Proximal Bifurcation model of Patient 3, are positive, which means the displacement force acts toward the front of the body.

2.4.3 Endograft Curvature

The curvature for all devices and their components is reported in

Table 2.12 - Table 2.15. The overall curvature range was 0.009 mm^{-1} to 0.028 mm^{-1} , with the Proximal Bifurcation design consistently having the lowest curvature when compared to the Mid and Distal Bifurcation designs. The curvature in the Mid Bifurcation case is equal to or greater when compared with the Distal Bifurcation device. The right limb curvature is always least in the Proximal Bifurcation model, greatest in the Distal Bifurcation Model and between the two in the Mid Bifurcation model. The same is true for the left limb curvature, with the exception of Patient 2, where the Mid Bifurcation curvature is slightly greater than the Distal Bifurcation model.

The total curvature of each device was compared to the force experienced by that device across the four patients. For a given patient, lower curvature values corresponded to lower total displacement forces and vice versa. The results are plotted in Figure 2.5.

Patient 1	Proximal Bifurcation	Mid Bifurcation	Distal Bifurcation
Curvature, Total	0.009	0.021	0.026
Curvature, Body	N/A	0.022	0.014
Curvature, Right Limb	0.006	0.017	0.026
Curvature, Left Limb	0.013	0.024	0.050

Table 2.12. Patient 1 curvature.

Patient 2	Proximal Bifurcation	Mid Bifurcation	Distal Bifurcation
<i>Curvature, Total</i>	<i>0.009</i>	<i>0.014</i>	<i>0.013</i>
Curvature, Body	N/A	0.010	0.010
Curvature, Right Limb	0.009	0.016	0.025
Curvature, Left Limb	0.008	0.015	0.012

Table 2.13. Patient 2 curvature.

Patient 3	Proximal Bifurcation	Mid Bifurcation	Distal Bifurcation
<i>Curvature, Total</i>	<i>0.009</i>	<i>0.018</i>	<i>0.024</i>
Curvature, Body	N/A	0.011	0.010
Curvature, Right Limb	0.010	0.013	0.017
Curvature, Left Limb	0.007	0.029	0.058

Table 2.14. Patient 3 curvature.

Patient 4	Proximal Bifurcation	Mid Bifurcation	Distal Bifurcation
<i>Curvature, Total</i>	<i>0.014</i>	<i>0.028</i>	<i>0.023</i>
Curvature, Body	N/A	0.020	0.010
Curvature, Right Limb	0.011	0.026	0.048
Curvature, Left Limb	0.017	0.034	0.059

Table 2.15. Patient 4 curvature.

Table 2.12 - Table 2.15. A centerline-based curvature (mm^{-1}) was calculated for each device model in the four patient anatomies. The total curvature was determined by a weighted average of each component curvature featured in the device. Since the body of the Proximal Bifurcation device does not lend itself to centerline-based analysis, no curvature value is listed for its body.

Endograft Curvature vs. Force

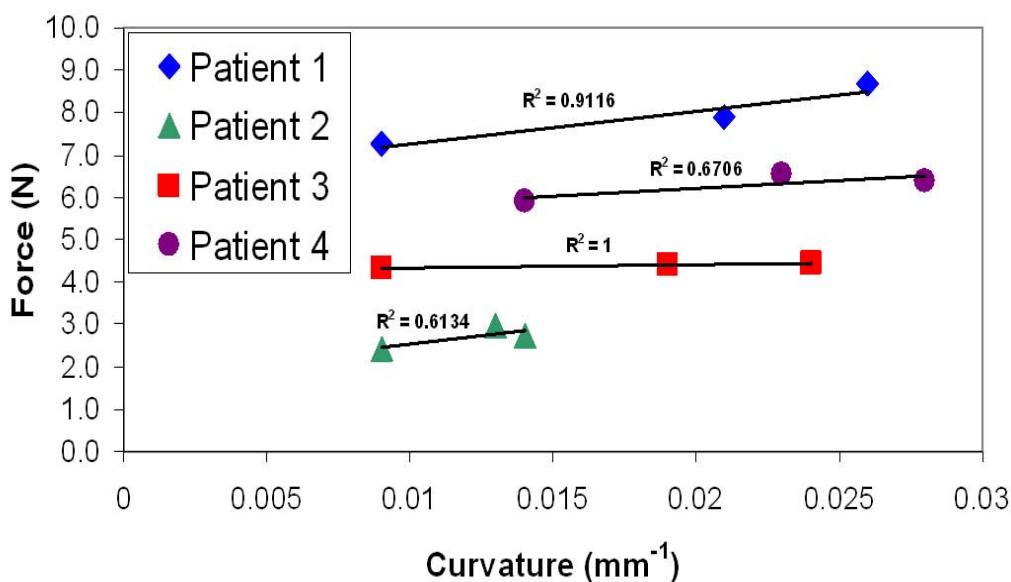


Figure 2.5. The total curvature of each device design is plotted versus the total displacement force acting on each device. The three data points for each patient represent the three device designs examined in this study. The correlation coefficient (R^2) is listed for each patient.

2.4.4 Surface Area of Endograft

The surface areas for all devices and their components are reported in Table 2.16 - Table 2.19 in units of mm². The total endograft surface area was always smallest in the Proximal Bifurcation device, ranging from 7,825 mm² to 10,418 mm². The Mid Bifurcation and Distal Bifurcation endograft surface areas were similar in all four patients, varying by as little as 15 mm² and by as much as 1,500 mm². The Right Limb and Left Limb surface area for a given device in a single patient varied by at most 763 mm², with a mean change of 686 mm² between the two limbs. The one exception is the models built for Patient 1, in which the Right Limb is significantly longer than the Left Limb (maximum difference in limb surface area is 2,376 mm²). The Body component of

the Proximal Bifurcation device is quite small, ranging from 262 mm² to 905 mm². The Body for this device refers to the shelf region generated by the unique design of the Proximal Bifurcation device.

The total surface area was compared to the total displacement force acting on the device, Figure 2.6. A correlation coefficient was calculated for all four patients, relating the three device designs to their respected displacement force. Lower surface areas tented to correspond to lower overall displacement forces, with Patient 3 exhibiting a nearly linear relationship between the surface area and the displacement force.

Patient 1	Proximal Bifurcation	Mid Bifurcation	Distal Bifurcation
Surface Area, Total	10,418	17,012	16,997
Surface Area, Body	905	5,976	10,249
Surface Area, Right Limb	4,911	6,706	4,456
Surface Area, Left Limb	4,602	4,330	2,292

Table 2.16. Patient 1 endograft surface area.

Patient 2	Proximal Bifurcation	Mid Bifurcation	Distal Bifurcation
Surface Area, Total	7,825	12,030	11,160
Surface Area, Body	262	5,201	7,277
Surface Area, Right Limb	3,693	3,347	1,621
Surface Area, Left Limb	3,870	3,482	2,263

Table 2.17. Patient 2 endograft surface area.

Patient 3	Proximal Bifurcation	Mid Bifurcation	Distal Bifurcation
<i>Surface Area, Total</i>	<i>9,067</i>	<i>13,970</i>	<i>15,423</i>
Surface Area, Body	432	5,590	10,706
Surface Area, Right Limb	4,292	3,952	2,054
Surface Area, Left Limb	4,343	4,427	2,663

Table 2.18. Patient 3 endograft surface area.

Patient 4	Proximal Bifurcation	Mid Bifurcation	Distal Bifurcation
<i>Surface Area, Total</i>	<i>8,871</i>	<i>10,180</i>	<i>9,781</i>
Surface Area, Body	330	3,644	6,424
Surface Area, Right Limb	3,889	3,167	1,515
Surface Area, Left Limb	4,652	3,369	1,842

Table 2.19. Patient 4 endograft surface area.

Table 2.16 - Table 2.19. The surface area of the device was calculated for all four patients across all three device cases. All values are reported in mm², and the components of the total surface area are also reported. In the case of the Proximal Bifurcation design, Body refers to the shelf created at the most proximal end of the implant, where the single lumen of the aorta becomes the double lumen of the endograft design.

Endograft Surface Area vs. Force

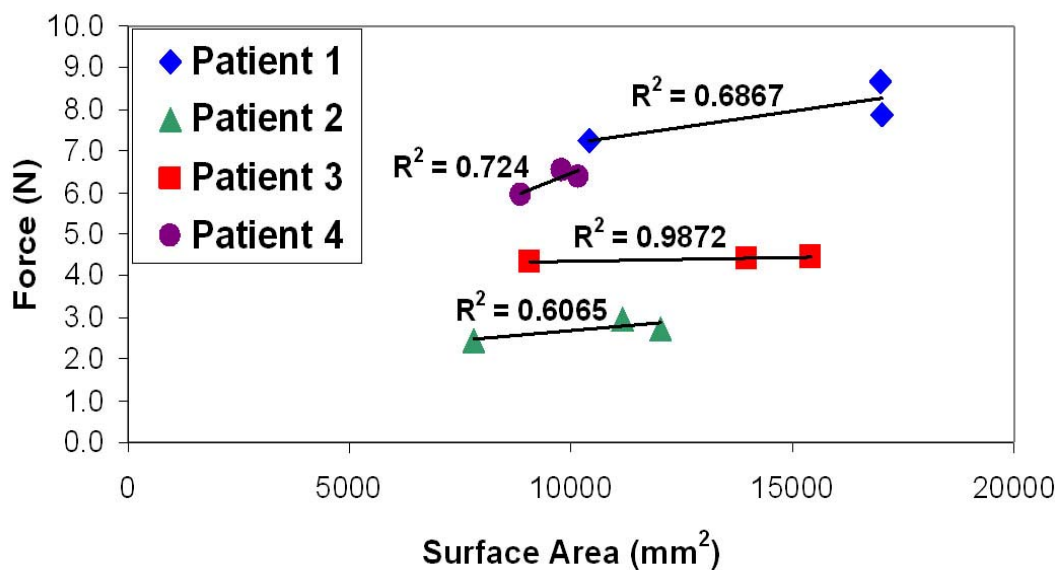


Figure 2.6. The total endograft surface area (mm²) in all three device designs is plotted versus the total force acting on the endograft. The correlation coefficient (R²) is listed for each patient.

2.5 Discussion

2.5.1 Pressures and Flow

The simulated pressures and flows agreed well with target pressures and flows, implying that the simulations accurately represent the pressure and flow environment in each patient. Further, there is little change in flow or pressure conditions from the Baseline model to each of the device models (Proximal Bifurcation, Mid Bifurcation and Distal Bifurcation). This means that there are no adverse pressure or flow changes due to the placement of an EVAR device. In addition, no one device demonstrated a consistent advantage over the others, based on pressure and flow conditions alone.

2.5.2 Displacement Force

The displacement forces calculated in this study are of similar magnitude reported by Figueroa, et. al. [39] and Howell, et. al. [30]. It should be further noted that the displacement forces were smallest for the Proximal, largest for Distal and in-between for the Mid Bifurcation models, which was true across all four patients analyzed. Aside from the endograft geometry, there are three factors impacting the total displacement force acting on the device: the patient's blood pressure, device curvature, and device surface area.

The patient's blood pressure plays a significant role in determining the displacement force magnitude experienced by an endograft. Patient 1 had the highest magnitudes of displacement force out of the four patients examined, and this patient also had the highest systolic and diastolic pressure readings. Similarly, Patient 2 (who had the lowest blood pressure in this study) produced the lowest overall values of displacement force. The relationship between increased patient blood pressure and higher displacement force is important to note because aneurysms are more common in hypertensive patients [45].

This study also found that increased curvature corresponds to increased magnitudes of displacement force acting on the device, as seen in Figure 2.5. By correlating the three device curvatures for each patient against the displacement force, the direct influence of curvature on displacement force is better quantified. The patient's blood pressure, which plays a defining role in generating the displacement force, remains the same in all three device designs simulated in a single patient. This result indicates that the curvature of the patient's anatomy influences the displacement force.

The findings also show that surface area defines the magnitude of the displacement force, with lower surface areas corresponding to lower generated displacement forces and vice versa, as seen in Figure 2.6. Since the force acting on the device was partially defined as the pressure acting over the endograft surface area, this finding is expected. It follows that devices with an overall smaller surface area will produce smaller displacement forces, when curvature and patient blood pressure is kept the same.

An interesting finding emerges when looking closer at the force exerted on the Body component of each device. Recall that the Body of the device was defined as the single-lumen segment from the proximal end of the device to where it bifurcated into the left and right limbs in the Mid and Distal Bifurcation models. In the Proximal Bifurcation model, the Body is defined as the shelf formed by the device as it splits into two lumens. The Body component of the overall displacement force is greatest for the Proximal Bifurcation model in only two of the four patients (Patients 1 and 3). The same two patients also have the largest Body (or shelf) surface area. Although intuitively it may seem that the presence of the device shelf will generate a substantial displacement force, most likely in the downward axial direction, this finding indicates that such is not always the case. The Proximal Bifurcation model of Patient 4, for instance, has a higher curvature than the Proximal Bifurcation models of the remaining patients, which may take away from the overall impact of the device shelf to the displacement force. The overall position of the device in the patient's anatomy as well as the local curvature and surface area will ultimately determine the effective displacement force contribution due to the Body feature in the Proximal Bifurcation design.

2.5.3 Device Segments

The Body segment of the Proximal Bifurcation device highlights an important difference between the impact of the static (due to the patient's blood pressure) and dynamic (due to the actual flow of blood) pressures on the overall displacement force. This geometry provides a shelf nearly perpendicular to normal blood flow, unlike the other two device designs where the transition from single to double lumens is considerably smoother. It is important to note that even though the vessel geometry undergoes a sudden change in cross sectional area (Proximal Bifurcation), the overall contribution to the displacement force is on par with the displacement force generated by the Body segments in the other two designs (Mid Bifurcation and Distal Bifurcation). This finding highlights the difference in impact between static and dynamic pressures. The static pressure has a much higher contribution to the overall force experienced by the device, rather than the dynamic pressure. If the dynamic pressure was a significant contributor to the total displacement force, considerable forces would be expected to act on the shelf surface. Although velocity may see significant changes on the local level with different device designs [46], velocity does not significantly impact the magnitude of the displacement force.

While understanding the displacement force magnitude and direction is an important clue in evaluating the design and safety of EVAR devices, some consideration should also be given to the types of anchoring mechanisms utilized by each device. For example, the Distal Bifurcation device straddles the iliac bifurcation. Therefore, there is little chance of its limbs migrating over time. For such a device, it may be appropriate to only take into account the displacement force imparted to the Body portion of the endograft.

2.5.4 Conclusion

Using computational fluid dynamics, the pressures, flows, displacement forces, curvatures and surface areas for three distinct device designs were calculated across four patient-specific anatomies. There is no indication of adverse pressure or flow effects after endograft placement and exclusion of the aneurysm to blood flow. Results show that curvature of the device, patient blood pressure, device surface area and location of the endograft bifurcation play an important role in dictating the magnitude of the displacement force.

2.5.5 Future Work

The findings highlighted in this study are limited by the small number of available data sets, and a more extensive study is needed to draw statistical inferences between graft design features and anatomical factors. The methods developed in this chapter can be expanded to study endografts for the treatment of thoracic aortic aneurysms (TAA's). Although TAA's are less common than AAA's, endovascular devices for the thoracic aorta are becoming more popular. Further, patients modeled in this study can be tracked during follow-up visits to measure the degree of device displacement, which can then be correlated to the displacement forces calculated.

3 Computational Modeling of Shear-Based Hemolysis Due to Renal Obstruction

3.1 Overview

As endovascular treatment of abdominal aortic aneurysms (AAAs) gains popularity, it's becoming possible to treat certain challenging aneurysmal anatomies with endografts relying on suprarenal fixation. In such anatomies, the bare struts of the device may be placed across the renal artery ostia, causing partial obstruction to renal artery blood flow. The obstructions create areas of high shear stress, which may lead to blood damage. Computational fluid dynamics (CFD) was used to simulate blood flow from the aorta to the renal arteries, utilizing patient-specific boundary conditions, in three patient models and calculate the degree of shear-based blood damage (hemolysis).

We used contrast-enhanced computed tomography angiography (CTA) data from three AAA patients who were treated with a novel endograft to build patient-specific models. For each of the three patients, a Baseline model and Endoframe model was constructed. The Baseline model was a direct representation of the patient's 30-day post-operative CTA data. This model was then altered to create the Endoframe model, which included a ring of metallic struts across the renal artery ostia. Computational fluid dynamics (CFD) was used to simulate blood flow, utilizing patient-specific boundary conditions. Pressures, flows, shear stresses and the Normalized Index of Hemolysis (NIH) were quantified for all patients.

The overall differences between the Baseline and Endoframe models for all three patients were minimal, as measured through pressure, volumetric flow, velocity, and shear stress. The average NIH across the three Baseline and Endoframe models was 0.002 and 0.004, respectively.

Results of CFD modeling show that the overall disturbance to flow due to the presence of the endoframe struts is minimal. The magnitude of the NIH in all models was well below the accepted design and safety threshold for implantable medical devices that interact with blood flow.

3.2 Background

Endovascular treatment of abdominal aortic aneurysms (AAAs) with endografts is gaining popularity in the clinical setting due to faster recovery times and a lower chance of mortality during the procedure when compared to traditional, open surgical repair [36], [10]. Not all patients, however, are candidates for this type of treatment. Some AAA anatomies are challenging to treat and rely on suprarenal fixation for anchoring and stability [31]. There is also evidence that suprarenal fixation is more stable than infrarenal anchoring, due to this region of the aorta being less likely to experience dilation [47], [46].

There are several FDA-approved endografts currently available in the U.S. market and many more devices in the developmental stage. Although there is considerable variation in the configuration of these devices, they always feature a metal scaffold (or endoframe) which is often covered by a graft material, such as Dacron. The graft material does not extend over the full length of the device body, and leaves some of the metal

struts of the endoframe exposed at the proximal end of the device. Utilizing suprarenal fixation requires the placement of these bare struts across the renal artery ostia.

The study presented here evaluates the degree of changes in blood flow and blood damage which may occur when an endograft is positioned such that the renal arteries are obstructed by the fabric-free, endoframe structure of the device. Using computational fluid dynamics (CFD), this work explores the hemodynamic and shear-based hemolysis effects of blood flow under such conditions.

3.3 Methods

3.3.1 Patient Data

Computed tomography angiography (CTA) data sets from three male patients with diagnosed abdominal aortic aneurysms (AAA's) were utilized in this study (Table 3.1). Patient A had a history of smoking and Patient C had a history of diabetes. The data sets were acquired from an anonymized database of patients who were treated with a novel endograft. All data sets were acquired at 30 days after intervention (Figure 3.1).

PATIENT SUMMARY	Age	Sex	Mass (kg)	Height (m)	Mosteller BSA (m ²)	HR (bpm)	Systolic BP (mm Hg)	Diastolic BP (mm Hg)
Patient A	68	Male	75	1.69	1.88	70	140	85
Patient B	59	Male	70	1.73	1.83	82	135	90
Patient C	64	Male	76	1.85	1.98	65	130	85
<i>Mean</i>	63.67	-	73.67	1.76	1.90	72.33	135.00	86.67
<i>St. Dev.</i>	4.51	-	3.21	0.08	0.07	8.74	5.00	2.89

Table 3.1. A demographic summary of the patients examined in this study, BSA is the body surface area in meters², HR is the heart rate in beats per minute and BP is the blood pressure in millimeters of mercury.

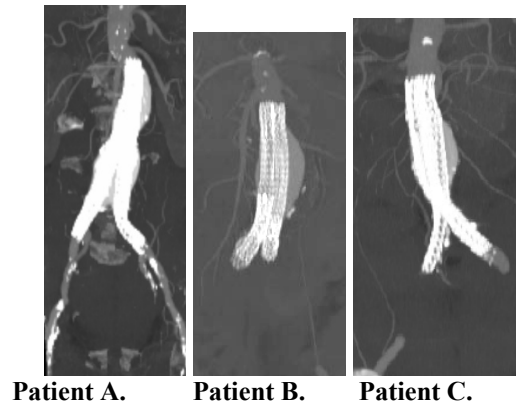


Figure 3.1. Maximum intensity projection (MIP) renderings of the CTA data sets used in this study for the three patients.

3.3.2 Model Construction

Three patient specific models were created for this study based on the CTA image data. The abdominal aorta of the three patients was segmented using custom software, simVascular [42]. In this approach, centerlines were created along the desired blood vessels which, in addition to the abdominal aorta, included the following arteries: hepatic, splenic, superior mesenteric, left renal, right renal, left external iliac, right external iliac, left internal iliac and right internal iliac. Cross sections of those vessels were generated along the centerline and then lofted together to represent the final patient geometry. The methodology is illustrated in Figure 3.2 for Patient A.

Although each of the patients in this study (Patients A-C) was treated with an endograft, none of the cases featured the device obstructing the renal artery ostia. Each patient model was therefore slightly altered as to simulate the bare endograft structure at the proximal end of the device placed across the renal artery ostia. The endoframe structure of the device was constructed using SolidWorks 2010 and then imported into each patient anatomy. The placement of the endoframe struts for each patient model can

be seen in Figure 3.3. Each patient dataset, therefore, yielded two models: Baseline model and Endoframe model. The Baseline model represented the unaltered patient anatomy and the Endoframe model featured a row of metal struts obstructing the renal artery ostia.

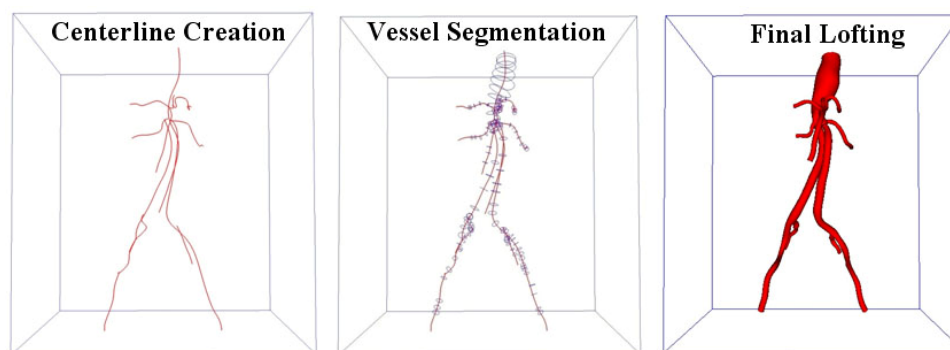


Figure 3.2. Geometric models were created for each patient based on CTA data using 2D segmentation techniques. In this method, centerlines were created along the desired vessels, which allowed for vessel segmentation. Finally, the vessel cross-sections were lofted together to generate the final geometric model.

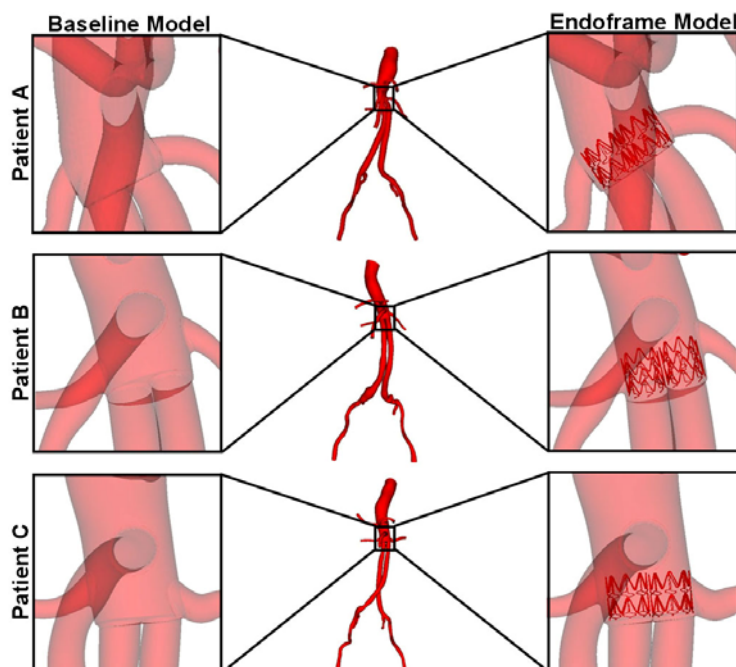


Figure 3.3. Each patient Baseline model was altered to include a row of metal scaffold struts obstructing the renal ostia. The additional set of models is referred to as Endoframe models and is depicted above.

3.3.3 Boundary Conditions

Volumetric inflow waveforms were prescribed at the inlet of each model based on a PC-MRI population study completed by Les, et. al. [4] and detailed in Eq. (3.1) and Eq. (3.2). The waveform was scaled in accordance with the morphometric parameters described in the population study using each patient's calculated body surface areas (BSA) according to the Mosteller formula [48], Eq. (3.3).

$$SCFlow_{mean} = 16.4(BSA)^{1.56} \quad (3.1)$$

$$IRFlow_{mean} = 3.98(BSA)^{2.00} \quad (3.2)$$

$$BSA = \sqrt{\frac{Height \times Weight}{36}} \quad (3.3)$$

The patient's mean supraceliac (*SCFlow*) and infrarenal volumetric (*IRFlow*) blood flows are quantified by Eq. (3.1) and (3.2), respectively, as a function of the body surface area. The following units were used in Eq. (3.1) - (3.3): mean volumetric flows are calculated in milliliters per second (ml/s), the BSA used is in square meters (m²), the height is in meters (m) and the weight is in kilograms (kg).

Since the blood flow in the entire vasculature of the human body is too complex to simulate, a lumped parameters model was used to represent the vasculature downstream of the geometric model [49]. Each model outlet was coupled to a three-element Windkessel or RCR model. The three parts of the model, R_p , C , and R_d , correspond to the resistance of the proximal arteries, the artery compliance and the distal resistance of the vascular bed, respectively. Initially, the values of the $R_p C R_d$ parameters were computed based on the patient's average blood pressure over the cardiac cycle, flow splits from literature [4], total resistance and total compliance. The RCR parameters were tuned

during the Baseline model simulation to coincide with the patient's recorded blood pressure and expected flow splits.

3.3.4 Simulation

Each patient's Baseline model was first discretized into a coarse isotropic finite-element volume mesh using a commercial meshing kernel (MeshSimTM, Simmetrix, Troy, NY). Each of the initial coarse meshes was composed of tetrahedral elements having a maximum edge size of 1 mm. Steady simulations were run with the predicted inflow based on patient body surface area and resistance outlet boundary conditions based on the patient's measured blood pressure and expected flow splits. When the desired pressures and flow conditions were reached, the results were used to run pulsatile simulations. For the pulsatile simulations, RCR outlet boundary conditions were utilized and adjusted such that the calculated pressure at the model inflow was within 5 percent of the patient's measured systolic and diastolic blood pressure. The flow to each outlet was also adjusted such that it was within 5 percent of the expected volumetric flow. The desired flow splits were accomplished by tuning the various parameters in the RCR boundary conditions. In general, increasing the capacitance (C) yielded a smaller pulse pressure (and vice versa) and increasing the total resistance (R) increased the blood pressure. It is important to note that the majority of the resistance at each vessel outlet is due to the downstream vasculature, representing the capillary bed. As such, 94.4 percent of the resistance at each vessel outlet was prescribed to R_{distal} , with the remaining amount assigned to R_{proximal} . The important exception to this resistance split is the renal arteries, which were assigned R_{distal} value 72 percent of R_{total} to account for the relatively low resistance of the kidneys'

vascular bed. The boundary conditions of the pulsatile simulation were adjusted until the desired inlet pressure and outlet flow was achieved. The last step in the simulation process was to create a final, locally-refined mesh with a local maximum edge size of 0.065 mm. The local refinement for the Baseline models was centered on the renal artery ostia and the Endoframe models were refined based on the location of the imported struts. The statistics for the final finite elements meshes are summarized in Table 3.2. The simulations were then run on the new refined meshes using the boundary conditions tuned on the coarse meshes.

FINAL MESH STATISTICS	Baseline Model	Endoframe Model
Patient A	2,416,417	4,593,143
Patient B	2,844,901	5,969,240
Patient C	3,212,083	5,580,734
<i>Average</i>	2,824,467	5,381,039
<i>St. Dev.</i>	398,226	709,450

Table 3.2. Total number of finite elements in each of the refined model meshes.

The pressure and velocity fields were calculated by solving the incompressible Navier-Stokes equations with a custom stabilized finite-element solver. The viscosity ($\mu=0.04$ P) and density ($\rho=1.06$ g/cm³) of blood were assumed to be constant and gravity was neglected. The walls of the models were defined to be rigid and a no-slip velocity condition was prescribed at the walls. The shape of the velocity profile was constrained at each outlet with an augmented Lagrangian method [39] to avoid divergence during retrograde flow. This method does not affect the overall amount of flow leaving each outlet, it simply constrains the shape. Eight cardiac cycles were computed for each model's simulation, to ensure convergence and an acceptably low residual or error in the

last five simulated cardiac cycles (cycle four through eight). All simulations were run with a time step of $1/1000^{\text{th}}$ of the cardiac cycle, with up to eight non-linear iterations per time step. The solution at every twentieth time step was saved, so that each cardiac cycle was represented at 50 time points. The same boundary conditions determined during the Baseline model simulations were applied to the Endoframe models. The pressure, velocity, and flow stresses were calculated for each of the six models examined in this study.

3.3.5 Reynolds Number

The mean and systolic Reynolds numbers were calculated for the left and right renal arteries, just distal of the renal ostia for both the Baseline and Endoframe models. Equations (3.4) and (3.5) were used to calculate the Reynolds numbers:

$$\text{Re}_{mean} = \frac{\rho 4 Q_{mean}}{\pi D_{mean} \mu} \quad (3.4)$$

$$\text{Re}_{systole} = \frac{\rho 4 Q_{systole}}{\pi D_{mean} \mu} \quad (3.5)$$

where ρ is the blood density (1.06 g/cm^3), Q_{mean} is the mean volumetric flow to the right or left renal artery over the cardiac cycle, $Q_{systole}$ is the peak volumetric flow to the right or left renal artery, D_{mean} is the mean diameter of the right or left renal artery, and μ is the dynamic viscosity (0.04 P).

3.3.6 Stress Tensor and Scalar Stress

The viscous stress tensor can be written in terms of the velocity gradient according to Eq. (3.6):

$$\overline{\sigma} = -\mu \begin{bmatrix} 2 \frac{\partial u}{\partial x} & \left(\frac{\partial u}{\partial y} + \frac{\partial v}{\partial x} \right) & \left(\frac{\partial u}{\partial z} + \frac{\partial w}{\partial x} \right) \\ \left(\frac{\partial u}{\partial y} + \frac{\partial v}{\partial x} \right) & 2 \frac{\partial v}{\partial y} & \left(\frac{\partial v}{\partial z} + \frac{\partial w}{\partial y} \right) \\ \left(\frac{\partial u}{\partial z} + \frac{\partial w}{\partial x} \right) & \left(\frac{\partial v}{\partial z} + \frac{\partial w}{\partial y} \right) & 2 \frac{\partial w}{\partial z} \end{bmatrix} \quad (3.6)$$

where $\overline{\sigma}$ is the viscous stress tensor and u , v , and w are the velocity components in the x-, y-, and z-directions, respectively. In addition to viscous stresses, turbulent effects were also accounted for by calculating the Reynolds stress term defined by Eq. (3.7):

$$\overline{\rho u_i u_j} = \begin{bmatrix} \overline{\rho u^2} & \overline{\rho uv} & \overline{\rho uw} \\ \overline{\rho uv} & \overline{\rho v^2} & \overline{\rho vw} \\ \overline{\rho uw} & \overline{\rho vw} & \overline{\rho w^2} \end{bmatrix} \quad (3.7)$$

The components of Eq. (3.7) were determined by analyzing the cycle to cycle variation in the velocity field for simulated cardiac cycles four through eight. An ensemble average of the velocity was calculated for the last five cardiac cycles of each simulation. A periodic average was then defined by extending the ensemble average to the same temporal domain as the original velocity field, in this case, the last five cardiac cycles. The velocity deviation term was defined as the difference between the original velocity field for a given cardiac cycle and the periodic average. The time averaged components of the Reynolds stress defined in Eq. (3.7) were computed by averaging the

velocity deviation term over the last five cardiac cycles (cycles four through eight) of each model's simulation.

By summing the viscous (Eq. (3.6)) and Reynolds (Eq. (3.7)) stress tensors, the final stress field, $\bar{\tau}$, was obtained for every node over each model's cardiac cycle. The stress analysis was simplified by calculating the scalar stress value at each node according to a method described by Bludszuweit [50] and defined by Eq. (3.8):

$$\tau_{scalar} = \left[\frac{1}{3} (\tau_{ii}^2 + \tau_{jj}^2 + \tau_{kk}^2) - \frac{1}{3} (\tau_{ii}\tau_{jj} + \tau_{jj}\tau_{kk} + \tau_{kk}\tau_{ii}) + (\tau_{ij}^2 + \tau_{jk}^2 + \tau_{ki}^2) \right]^{1/2} \quad (3.8)$$

3.3.7 Normalized Index of Hemolysis

The Normalized Index of Hemolysis (NIH) is a measure of the amount of blood damage caused by shear stresses found in a given flow domain. The NIH [51], in units of $\frac{g}{100L}$, is quantified according to the Eq. (3.9) below:

$$NIH = 100 \times \frac{\Delta Hb}{Hb} \times (1 - Hct) \times \kappa \quad (3.9)$$

where $\frac{\Delta Hb}{Hb}$ is the change in hemoglobin content of the blood, Hct is the hematocrit count (40 percent for this study), and κ is the hemoglobin content of blood ($1.5 \frac{g}{100L}$) for this study). There are several models for the change in hemoglobin due to shear stress in a flow field [52], [53], [54], [55], and Giersipien's empirical model [55] was selected for this study. This model tracks the change of hemoglobin ($\frac{\Delta Hb}{Hb}$) according to the following equation:

$$\frac{\Delta Hb}{Hb} = 3.62 \times 10^{-7} \tau^{2.416} \Delta t^{0.785} \quad (3.10)$$

where τ is the stress and Δt is the amount of time blood experiences that stress.

In order to calculate the change in hemoglobin defined by Eq. (3.10), 200 particles were released into the flow at the inlet of each model. The path of those particles was calculated and the corresponding stress, as defined by Eq. (3.8), for a given location and time was recorded over the last cardiac cycle. For each of the particles, the total $\frac{\Delta Hb}{Hb}$ term was found by integrating over the calculated pathlines. The final $\frac{\Delta Hb}{Hb}$ value for each model was the average change in hemoglobin across all 200 generated pathlines.

3.4 Results

3.4.1 Pressure and Volumetric Flow

The pressure computed at each Baseline model's inflow face agreed well with the respective patient's measured systolic and diastolic pressures, as can be seen in Fig. 4. The inlet pressure calculated for each of the three Endoframe patient models corresponded closely to the waveform shown for the Baseline model. The difference between the simulated and measured pressure pulse was less than 5 percent in all cases. The simulated volumetric flows at the nine vessel outlets of all models were also within 5 percent of the target volumetric flows. The flows to each outlet agreed well in the Baseline and Endoframe model for each of the patients examined, at most differing by 0.2 ml/sec.

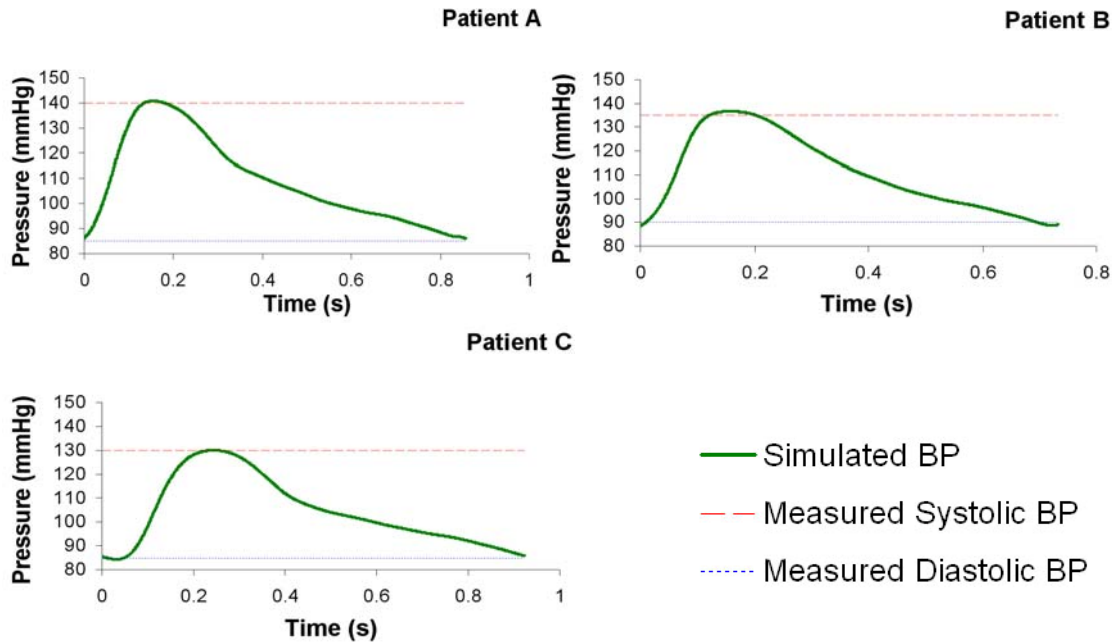


Figure 3.4. Pressure waveforms (green, solid line) at the inlet were computed for each patient anatomy. The measured systolic (red, dashed line) and diastolic (blue, dotted line) patient blood pressures are also displayed. There was no noteworthy difference in the inlet blood pressure between the Baseline and Endoframe models for a given patient. The pressure waveform maximums and minimums (green, solid line) were within 5% of the measured systolic (red, dashed line) and diastolic (blue, dotted line) blood pressure values, respectively.

3.4.2 Reynolds Number

The average Reynolds numbers for the right and left renal arteries, computed just distal to the ostia, across all three patients were 1,618 and 1,499, respectively, during peak flow. With average flow, the average Reynolds values drop to 419 and 388, respectively, as summarized in Table 3.3.

REYNOLDS NUMBER	Right Renal Artery		Left Renal Artery	
	Peak Flow	Average Flow	Peak Flow	Average Flow
Patient A	1,354	351	1,309	339
Patient B	1,900	486	2,031	520
Patient C	1,601	420	1,157	304
<i>Average</i>	<i>1,618</i>	<i>419</i>	<i>1,499</i>	<i>388</i>
<i>St. Dev.</i>	<i>273</i>	<i>68</i>	<i>467</i>	<i>116</i>

Table 3.3. Computed Reynolds numbers for flow into the renal arteries, just distal to the renal ostia, for peak and average flow over the cardiac cycle.

3.4.3 Velocity

The velocity was calculated over the domain of each of the six models (three Baseline and three Endoframe), with volumetric renderings of the velocity magnitude in peak systole seen in Figure 3.5. On the whole, the velocity distribution was similar between the Baseline and Endoframe simulations in each of the three patients. Patient A displayed high velocity magnitudes in the hepatic, celiac and superior mesenteric arteries. High velocity magnitudes could also be seen in the distal portions of the external iliac arteries. The proximal end of the model, where the diameter of the aorta is the largest, consistently displayed lower velocity values. Patient B showed similar velocity magnitude trends to patient A, but the velocity in the proximal abdominal aorta and both of the renal arteries was higher. Finally, Patient C exhibited high velocity magnitudes in most of the models' branch vessels, including: hepatic artery, splenic artery, superior mesenteric artery, both renal arteries and both external iliac arteries.

Although the overall trends in the velocity magnitudes agreed well between the Baseline and Endoframe models in all three patients, a clear difference is seen in the areas around the struts of the endoframe. Diminished velocity values outline the cross-sectional areas of the endoframe struts, as seen in the enlarged cross-sectional slices of

Figure 3.5. The velocity magnitudes close to the spatial position of the endoframe struts differ between the Baseline and Endoframe models, but begin to exhibit the same velocity characteristics further away from the endoframe struts.

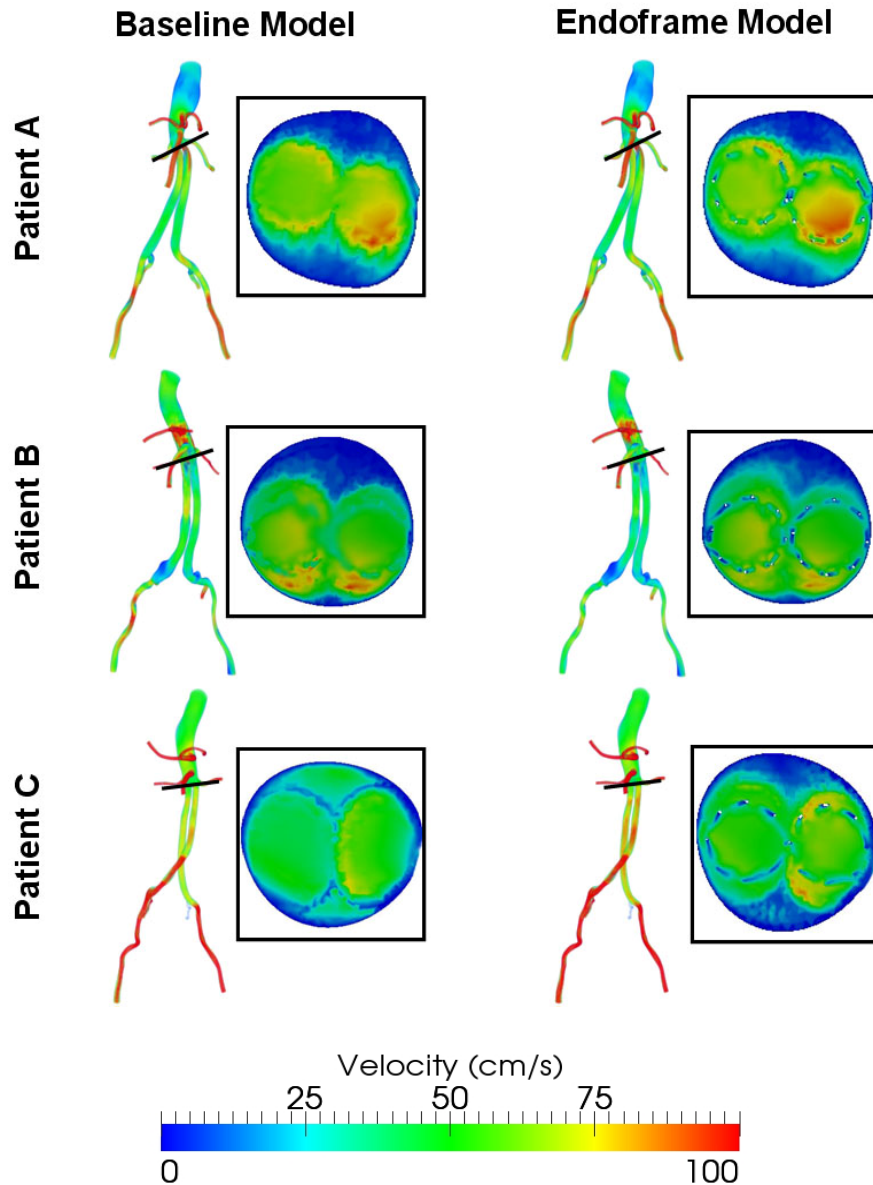


Figure 3.5. Volume rendering of the velocity magnitude (cm/s) in peak-systole for the Baseline and Endoframe models in all three patients. Velocities at a cross-section immediately distal to the renal artery ostia are also illustrated in a magnified view.

3.4.4 Stress

Figure 3.6 illustrates the stress domain in peak systole for the Baseline and Endoframe models for all three patients. Overall, the stress domains were similar for each of the patient's two models. The lowest overall scalar stresses were found in the proximal abdominal aorta and higher stress values were generally found in the branch vessels. Patient C displayed higher overall scalar stress values in its limbs than the other two patients.

Very distinct differences in the stress magnitude distribution are present in the immediate vicinity of the endoframe struts, as seen in the magnified cross-sections of Figure 3.6. In all Endoframe models, elevated levels of scalar stress are found close to the endoframe features. The stress in the Endoframe models decreases further away from the endoframe struts and the scalar stress field begins to resemble its Baseline model counterpart. One exception to this trend is Patient B, who experiences moderate shear along the posterior wall and low shear along the anterior wall of the abdominal aorta in the Baseline model. This trend is reversed in the Endoframe model.

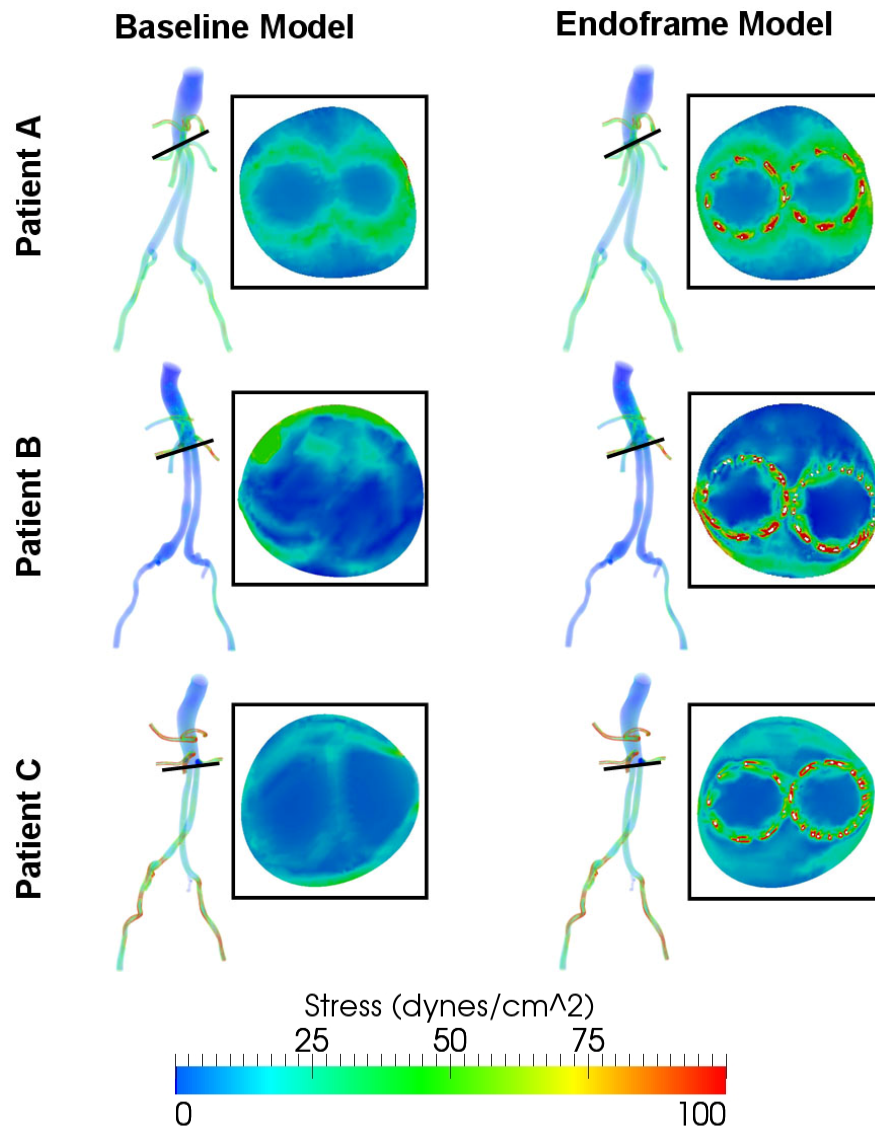


Figure 3.6. Volume rendering of the scalar stress field of the Baseline and Endoframe models for Patients A - C. Stress field at a cross-sectional level immediately distal to the renal artery ostia is also illustrated in a magnified view. Elevated levels of stress can be seen around the endoframe struts for all Endoframe models.

3.4.5 Normalized Index of Hemolysis

The computed NIH is shown for all six models in Table 3.4. The NIH of Baseline models were consistently lower than their Endoframe counterparts. For Patients A and B, the Endoframe model NIH was twice as large as the Baseline model NIH. Patient B had the highest overall NIH for each of its models.

NIH	Baseline Model	Endoframe Model
Patient A	0.001	0.002
Patient B	0.003	0.006
Patient C	0.001	0.004
<i>Average</i>	<i>0.002</i>	<i>0.004</i>
<i>St. Dev.</i>	<i>0.001</i>	<i>0.002</i>

Table 3.4. Computed NIH values (g/100 L) for all six patient models.

3.5 Discussion

3.5.1 Pressure and Flow

The pressures and volumetric flows simulated in this study agreed well with the patients' measured blood pressure and target volumetric flow splits. This indicates that the pressure and flow domains in each patient are well represented. Since the pressure wave at the inlet of each patient's Baseline model matched well with the pressure at the inlet of its Endoframe model, that there are no undesirable pressure changes due to the presence of the endoframe struts. The volumetric flow measured in each pair of patient models is also closely matched, indicating that flow to the renal arteries is unaffected by the partial blockage of the renal artery ostia. At no point during the cardiac cycle do the renal arteries experience retrograde flow, which is consistent with what is known about blood flow to the kidneys [56].

3.5.2 Reynolds Number

The Reynolds number, calculated just distal of the renal ostia, in all models placed the flow conditions to be below the turbulent threshold. This shows that viscous forces play a dominant role in renal flow, with and without the placement of the metal struts. Since the volumetric flow to the renal arteries was virtually unchanged between the Baseline and Endograft models, the Reynolds number was the same for both cases across all patients.

3.5.3 Velocity

The velocity distribution is similar in each pair of Baseline and Endoframe models, with notable differences only in the immediate vicinity of the endoframe struts. Each strut is bordered by an area of low velocity, due to the no-slip condition applied at the device surface. In regions further away from the struts, similar distributions in velocity magnitude are seen. This indicates that placement of the endoframe struts across the renal artery ostia cause a local disturbance in the velocity magnitude, but ultimately do not have a significant overall effect on the velocity.

3.5.4 Stress

Areas of high stress are observed near the endoframe struts in all models, providing regions where red blood cells may have a higher chance of undergoing hemolysis. High stress values are also observed in the branch vessels of most models, with Patient C exhibiting particularly elevated levels of stress. This is likely due to the fact that the patient has a larger body surface area (1.98 m²) when compared to the Patient A (1.88

m²) and Patient B (1.83 m²). A larger BSA corresponds to a larger inflow volume which will translate to increased velocity yielding a higher stress in the fluid domain. It is interesting to note that the elevated stress found around the endoframe struts is still about twice the magnitude of the stress found in the branch vessels of Patient C. This indicates that the presence of the metallic strut introduces levels of flow stress not normally found in the patient's anatomy.

3.5.5 Normalized Index of Hemolysis

According to ASTM standard F1841-97/F1830-97 [57], Table 3.5, the NIH should be below 0.01 for an implantable device. All NIH values calculated in this study fall into that category. Although the presence of the endoframe struts introduces local areas of high stress, their overall effect on hemolysis is not significant. Studies suggest [40] that exposure to extremely high shear stress for short amounts of time does no significant damage to the red cells. Instead, it is prolonged exposure to moderate shears that is the driving factor in red blood cell destruction. Since red blood cells travel in the renal arteries at relatively high velocities, they are inevitably exposed to the high stress areas around the endoframe struts for a short amount of time.

NIH	Clinical Outcomes
>0.06	Increased levels of PfHb
>0.04	No increase of PfHb but blood transfusion required
<0.04	Physiologically acceptable
<0.02	Clinically acceptable
<0.01	Design objective

Table 3.5. ASTM standard F1841-97/F1830-97 classification of NIH levels and potential effects on clinical outcomes.

There is a dearth of computational studies to address the fluid mechanics implications of placing an obstruction across the renal artery ostia, and this work is an attempt to broaden the field. In addition to evaluating the degree of blood damage due to suprarenal fixation, the findings in this study are also applicable to evaluating the safety of other devices which may cross the renal arteries.

3.5.6 Biological Factors

Besides understanding the fluid mechanic implications of device positioning near the renal arteries, biological factors are also important when evaluating the safety of such device placement. Porcine studies with stents placed across the renal artery ostia report neointima forming on some device struts and in a number of cases filling the area between device struts [58], [59]. A rise in serum creatinine levels was also reported. The long-term implications of placing stent struts across the renal arteries have not been widely explored.

3.5.7 Conclusion

Results of CFD modeling of blood flow through patient-specific AAA anatomies with renal ostia partially obstructed by endoframe struts indicate that the overall disturbance to flow is minimal, as measured through pressure, volumetric flow, velocity, and shear stress. The NIH was at least twice as high in the Endoframe models as in the Baseline models due to the high flow stresses found in the immediate vicinity of the device struts.

However, the magnitude of the NIH in all models was well below the accepted design threshold for cardiovascular devices, as defined by ASTM standard F1841-97/F1830-97.

3.5.8 Future Work

The methods used in this study to quantify blood damage can be expanded to other implantable devices, such as blood pumps and ventricular assist devices. These devices typically experience much higher levels of stress than those found in this study, and are therefore more likely to induce blood damage. In addition, these studies can be supplemented with animal work to highlight the biological factors influencing hemolysis.

4 Shear-Based Red Blood Cell Damage Due to Flow Obstruction

4.1 Overview

Benchtop experiments studying blood damage (hemolysis) due to shear stress have been widely researched for high flow devices, such as blood pumps. Devices that cause passive obstructions to blood flow, such as those that may occur when stents or structural elements of endografts are placed across the renal arteries have not been explored, and this work aims to characterize the blood damage incurred in such scenarios.

Samples at 40 percent hematocrit were prepared from whole blood drawn from healthy patients. After washing the sample three times, red blood cells (RBC's) were extracted and suspended in a phosphate buffered saline (PBS) solution. Each sample was used within 24 hours of the initial drawing.

An experimental setup consisting of a peristaltic pump, collection capsule, and tubing of varying internal diameters was assembled in this study. The three sections of tubing were: inflow tube, pump tube and outflow tube. The internal diameter of each, respectively, was: 0.150 cm, 0.200 cm and 0.018 cm. The small internal diameter of the outflow tube allowed to high shear stresses during flow in this part of the circuit.

Two flow regimes were used in this study: Low Flow (0.0025 ml/s) and High Flow (0.086 ml/s). The shear generated by these flows in the Outflow Tube corresponded to the average (116 dynes/cm²) and high (4010 dynes/cm²) stresses found in the renal arteries in the previous chapter. The flow circuit also included a removable stainless steel mesh

across the inlet of the Outflow Tube to represent a flow obstruction due to an implantable device. The flow circuit was studied under four conditions: High Flow and Low Flow, each with and without the stainless steel mesh. Comment on stainless steel mesh dimensions and how they compare to Endoframe strut dimensions.

Samples from the flow circuit were drawn at four time points (10, 10^2 , 10^3 and 10^4 seconds) and analyzed for their cell content using the Advia 120 Hematology System, which relies on laser scattering techniques to determine the cells present in a given sample.

Results show that RBC's were virtually unaffected during Low Flow with and without the mesh. High Flow conditions with and without the mesh demonstrated significant level of RBC destruction during the last two time steps (10^3 and 10^4 seconds). In addition, the High Flow regime with mesh showed the creation of RBC fragments, which had a lesser incidence without the mesh. RBCs fragment were not detected during either of the Low Flow regimes.

4.2 Background

Shear-based blood damage (hemolysis) has been studied using viscometers, pumps and other custom benchtop models [40, 60, 61]. The aim of these studies has often been to evaluate the degree of blood damage created by blood pumps or artificial heart valves. No experimental work has been done to evaluate how a stationary obstruction to flow may influence red blood cells. Some implantable devices, such as AAA endograft, rely on suprarenal fixation thereby allowing metal struts to partially obstruct flow to the renal

arteries. This study is a first step in creating a benchtop model to evaluate the degree of hemolysis due to the presence of an obstruction to blood flow.

4.3 Methods

4.3.1 Sample Preparation

Blood drawn from healthy subjects was used in all experiments completed for this study. Every blood sample was mixed with the anticoagulant sodium polyanethenol sulfonate (SPS) and used within 24 hours of the initial drawing. Each sample of whole blood was washed three times with phosphate buffered saline (PBS) to isolate the erythrocytes, also known as red blood cells (RBCs), and eliminate the majority of plasma, leukocytes (white blood cells) and thrombocytes (platelets). The concentrated RBCs were then suspended in PBS to achieve a hematocrit level of 40 percent (± 2 percent). This level of hematocrit is comparable to that found in human whole blood, with men having a slightly higher hematocrit (45 percent) than women (40 percent) [62]. In addition, the blood flow simulations described in Chapters 2 and 3 were run assuming a hematocrit of 40 percent. The PBS solution provides a good osmolarity and ion concentration match to human blood, making it an excellent environment for RBCs. Each baseline sample was analyzed using the Advia 120 Hematology System (Siemens Healthcare Diagnostics, Deerfield, IL) to determine the initial sample RBC count and, therefore, level of hematocrit. A sample volume of 1.5 ml was then loaded into the flow circuit.

4.3.2 Flow Circuit

The flow circuit used in this study consisted of several sections of tubing, a collection capsule and a Rabbit Peristaltic Pump (Rainin Instruments Co, Woburn, MA) connected in series. Both the inflow and outflow tubing fed into the collection capsule to complete the circuit. The inflow tube was made of Tygon® and measured 50 cm in length with an inner diameter of 0.15 cm. This tubing was connected via luer and high-pressure fittings to a 15 cm length (inner diameter of 0.2 cm) Tygon® tube fitted to the peristaltic pump. Tygon has been shown to be non-hemolytic and is often used in medical applications with peristaltic pumps. The final section of tubing was a 50 cm long segment of outflow tubing made of polyetheretherketone (PEEK) with an inner diameter of 0.018 cm. The small inner diameter of the outflow PEEK tubing allowed to create significant levels of shear inside this section of the circuit, while the rest of the tubing imparted minimal shear on the blood. The outflow PEEK tubing fed into the same collection capsule, such that blood would continue to circulate throughout the system, as seen in Figure 4.1.

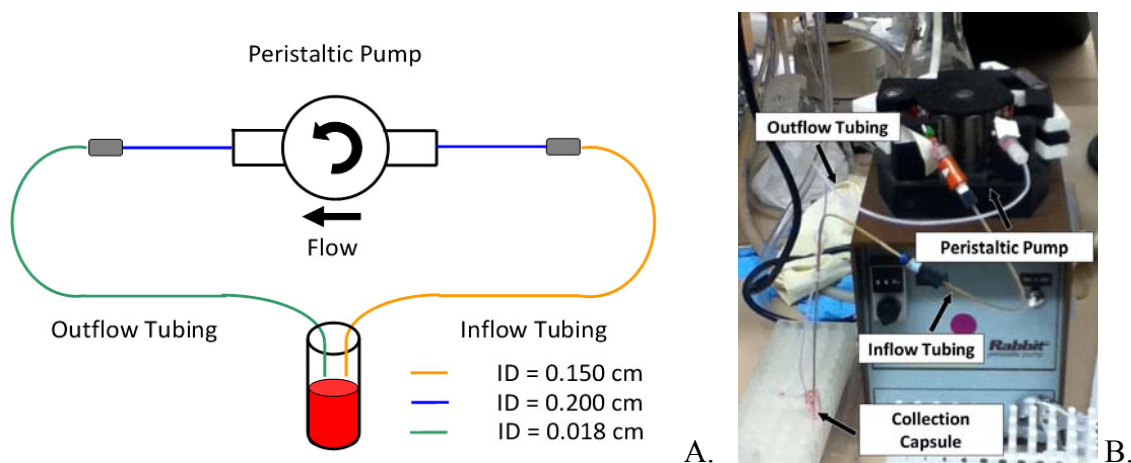


Figure 4.1. A schematic representation of the flow circuit is depicted in A., where three tubing segments of various diameter are connected in series and flow through the circuit is powered by a peristaltic pump. A photo of the flow circuit is shown in B.

After loading each sample into the collection capsule, the pump was turned on at a flow rate of 0.5 $\mu\text{l/s}$ and blood was allowed to fill the circuit such that no air remained inside the tubing. Circulating the blood at this low flow rate allowed to initialize each experiment with minimal damage to the RBCs. The flow rate was then increased to either 0.0025 ml/s (Low Flow) or 0.086 ml/s (High Flow). Blood samples were extracted from the circuit at 10, 10^2 , 10^3 and 10^4 seconds for each flow regime and analyzed with the Advia 120 Hematology System. The same steps were repeated after the circuit was altered to include a fine stainless steel mesh (wire diameter was 36 microns, distance between wires was 43 microns) at the PEEK tubing inlet. In total, four flow schemes were completed in this study: Low Flow without mesh, Low Flow with mesh, High Flow without mesh and High Flow with mesh.

4.3.3 Shear Stress Calculations

Two flow rates were used in the experimental setup to achieve two different levels of shear stresses acting on the fluid inside the circuit. The velocity profile along the z-axis for fully developed flow in a straight cylinder is defined in Eq. (4.1) as:

$$v_z(r) = -\frac{dP}{dz} \frac{1}{4\mu} (R^2 - r^2) \quad (4.1)$$

where v_z is the fluid velocity along the z-axis, $\frac{dP}{dz}$ is the change in pressure along the z-axis, μ is the dynamic viscosity, R is the radius of the cylinder and r is the spatial position along the r-axis. If a cylinder of length L is considered, then the change in pressure from one end of the cylinder to the other can be written as:

$$\frac{dP}{dz} = \frac{p_1 - p_2}{L} \quad (4.2)$$

where, p_1 is the pressure at the cylinder inlet, p_2 is the pressure at the cylinder outlet and L is the total length of the cylinder. By assuming that $\Delta p = p_2 - p_1$ and $p_1 > p_2$, providing a driving pressure to the cylinder flow, the velocity profile as described in Eq. (4.1) can be re-written as:

$$v_z(r) = -\frac{\Delta P}{L} \frac{1}{4\mu} (R^2 - r^2) \quad (4.3)$$

It is well noting that v_z remains positive as long as $p_1 > p_2$. Given the velocity profile of Eq. (4.3), the total flow in the cylinder can be determined by integrating over the cross-sectional area to obtain:

$$Q = \int_0^{2\pi} \int_0^R v_z(r) r dr d\theta \quad (4.4)$$

$$Q = -\frac{\pi R^4}{8\mu} \frac{\Delta p}{L} \quad (4.5)$$

where Q is the volumetric flow in the cylinder. Re-arranging Eq. (4.5), the velocity profile, previously described by Eq. (4.3), can be re-written in term of Q , thus eliminating the pressure term:

$$v_z(r) = \frac{2Q}{\pi R^4} (R^2 - r^2) \quad (4.6)$$

In viscous flow, the stress acting on the surface of an arbitrary volume can be described by the stress tensor:

$$\boldsymbol{\tau} = \begin{bmatrix} \tau_{rr} & \tau_{r\theta} & \tau_{rz} \\ \tau_{\theta r} & \tau_{\theta\theta} & \tau_{\theta z} \\ \tau_{zr} & \tau_{z\theta} & \tau_{zz} \end{bmatrix} \quad (4.7)$$

The components of this stress tensor in cylindrical coordinates are as follows:

$$\tau_{rr} = -p + 2\mu \frac{\partial v_r}{\partial r} \quad (4.8)$$

$$\tau_{\theta\theta} = -p + 2\mu \left(\frac{1}{r} \frac{\partial v_\theta}{\partial \theta} + \frac{v_r}{r} \right) \quad (4.9)$$

$$\tau_{zz} = -p + 2\mu \frac{\partial v_z}{\partial z} \quad (4.10)$$

$$\tau_{r\theta} = \tau_{\theta r} = \mu \left[r \frac{\partial}{\partial r} \left(\frac{v_\theta}{r} \right) + \frac{1}{r} \frac{\partial v_r}{\partial \theta} \right] \quad (4.11)$$

$$\tau_{\theta z} = \tau_{z\theta} = \mu \left(\frac{\partial v_\theta}{\partial z} + \frac{1}{r} \frac{\partial v_z}{\partial \theta} \right) \quad (4.12)$$

$$\tau_{rz} = \tau_{zr} = \mu \left(\frac{\partial v_r}{\partial z} + \frac{\partial v_z}{\partial r} \right) \quad (4.13)$$

The shear stresses in viscous flow are represented by Eq. (4.11) - Eq.(4.13), and only Eq. (4.13) becomes relevant for flow along the z-axis in the flow circuit. In fact, since there is no flow along the r-axis. Eq. (4.13) can be simplified to:

$$\tau_{rz} = \tau_{zr} = \mu \frac{\partial v_z}{\partial r} \quad (4.14)$$

This definition allows for describing the shear stress in the flow circuit in terms of the velocity in the z-direction. Using Eq. (4.6), the shear stress can be written as:

$$\tau = -\mu \frac{4Qr}{\pi R^4} \quad (4.15)$$

Given the above (Eq. (4.15)) definition for shear stress, the average shear stress experienced by fluid in a cylinder can be defined as:

$$\tau_{ave} = \frac{1}{\pi R^2} \int_0^R \tau(2\pi r) dr \quad (4.16)$$

$$\tau_{ave} = -\frac{8Q\mu}{3\pi R^3} \quad (4.17)$$

The above (Eq. (4.17)) relationship between shear stress and volumetric flow was used to define two different flow regimes 0.0025 ml/s (Low Flow) or 0.086 ml/s (High Flow).

Shear stress for various flow and ID values		Tubing ID (cm)		
		1.50E-01	2.00E-01	1.80E-02
Volumetric Flow (cc/s), Q	Q = 2.50E-03	2.01E-01	8.49E-02	1.16E+02
	Q = 8.60E-02	6.92E+00	2.92E+00	4.01E+03

Table 4.1. The above table summarizes the two types of flow used in the study and the resulting shear stress in the three different tube geometries.

4.3.4 Advia 120 Hematology System

The Advia 120 Hematology System is an automatic hematology analyzer able to perform complete blood counts, white blood cell differentials, and reticulocyte analysis. The system uses a series of chemical reactions to alter the shape of cells in a given sample, so that shape is eliminated as a variability factor. All cells are isovolumetrically expanded to assume a spherical shape, which is referred to as sphering. The reagents that

cause sphering include sodium dodecyl sulfate (SDS) and glutaraldehyde. Once the reaction is complete, cells are fixed.

An optical method is used to counting and charactering the cells in a given blood sample. In this method, simultaneous measurement of light scattered at a low angle (2° - 3°) and high angle (5° - 15°) is recorded. The scatter generated by the low angle measures the cell volume, while the high angle scatter characterizes hemoglobin concentration. Mie's theory of light scatter is used to convert the angle measurements into a scatter cytogram [63]. A schematic diagram of the Advia 120 Hematology System is pictured in Figure 4.2.

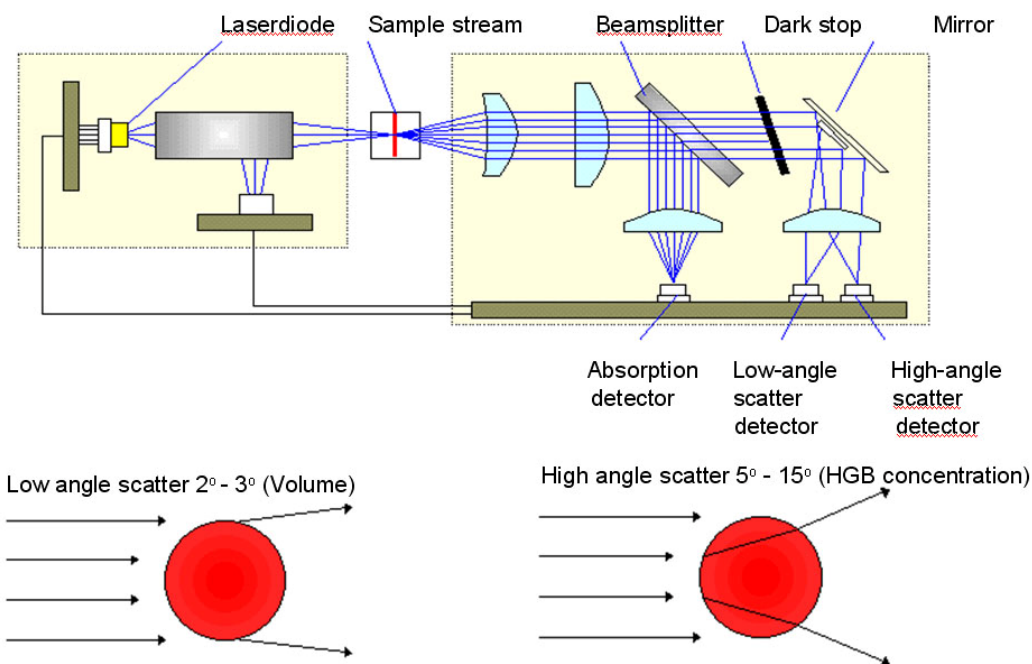


Figure 4.2. The ADVIA 120 Hematology system uses light scattered from a laser to analyze the cells present in a given sample. Low angle light scatter is measured to quantify the volume of a cell and high angle light scatter is used to describe the hemoglobin concentration present in a given sample.

Once the sample analysis is complete, a numerical count of RBC's is generated. In addition, a Volume/Hemoglobin Concentration (V/HC) cytogram is created for each sample, which is a graphical analysis of the sample's cell content. The hemoglobin

concentration is plotted along the x-axis and the cell volume is plotted along the y-axis. For a normal RBC, the hemoglobin concentration will fall between 28 and 41 g/dL, while the volume will measure between 60 and 120 fL. A sample V/HC cytogram for normal RBC's is pictured in Figure 4.3.

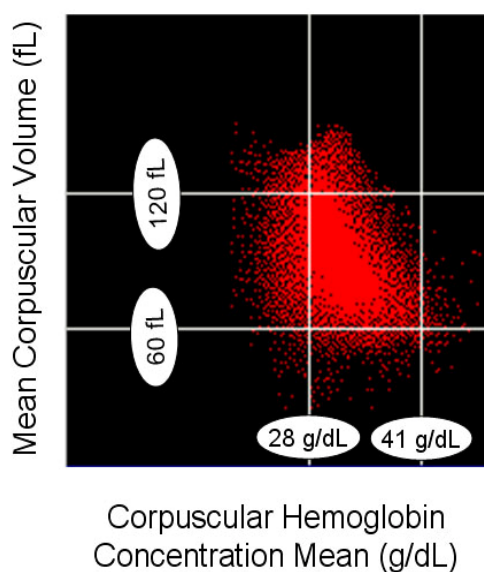


Figure 4.3. A Volume/Hemoglobin Concentration cytogram generated by the ADVIA 120 using a normal RBC sample. Hemoglobin concentration in (g/dL) is plotted along the a-axis and the cell volume is plotted along the y-axis (fL).

4.4 Results

4.4.1 Cell Counts

The RBC concentration was measured at the start of each of the four flow schemes and at varying time points, as seen in Figure 4.4. The RBC concentration in the High Flow regimes dropped with increasing time with and without the mesh. In contrast, the RBC concentration in the Low Flow regime stayed relatively constant over the entire length of the time exposure. At the 1,000 and 10,000 second time points, both of the Low

Flow regimes (with and without mesh) are significantly different from the High Flow regimes (with and without mesh). At the last time point (10,000 seconds) during the High Flow regime, nearly all RBC's are destroyed. The presence of the mesh did not impact the overall red blood cell concentration.

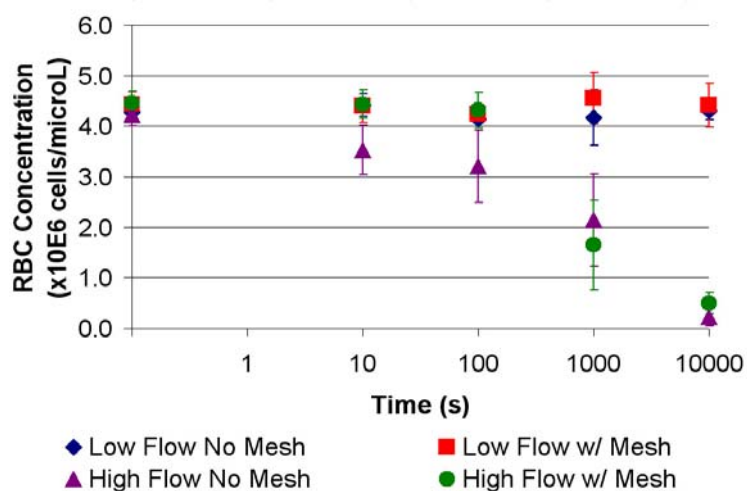


Figure 4.4. Blood samples were analyzed in four different flow regimes using a combination of Low Flow (0.01 ml/s) and High Flow (0.1 ml/s) as well as a stainless steel mesh (wire diameter was 36 microns, distance between wires was 43 microns). Samples were analyzed for RBC concentration at five distinct time points.

In addition to recording the presence of RBC, the cell characterization also recorded the presence of RBC fragments in each sample. The RBC fragments are tracked in each blood sample over time, as seen in Figure 4.5. In this case, the RBC fragment volume stayed fairly constant when no mesh was inserted into the flow circuit. Significant changes start to take place after 1,000 seconds. At this time point, the High Flow with Mesh regime sees the greatest amount of RBC fragment volume with High Flow without mesh regime also showing an increase in the generation of this type of cell. Both of the Low Flow regimes remain unchanged during this and the subsequent time point. At the last recorded time point, 10,000 seconds, the difference between High Flow with Mesh, High Flow, and the two Low Flow regimes is even more exaggerated.

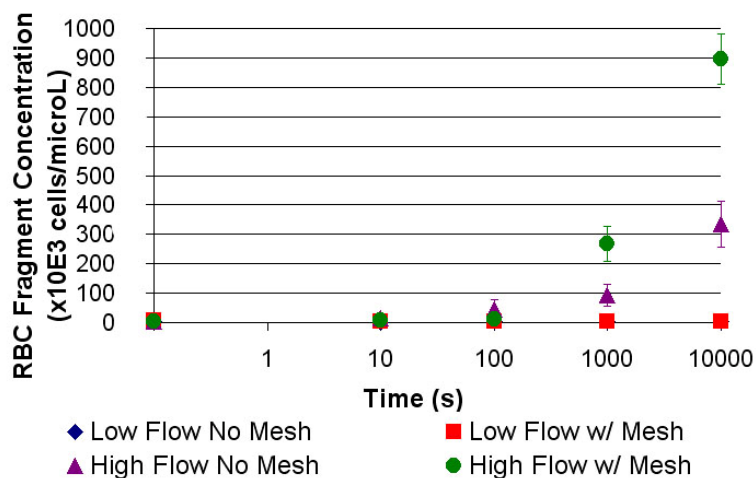


Figure 4.5. Four flow schemes were analyzed in this study incorporating Low Flow (0.01 ml/s) and High Flow (0.1 ml/s) with and without a stainless steel mesh (wire diameter was 36 microns, distance between wires was 43 microns). The mean RBC fragment volume was recorded at five time points in each flow experiment.

4.4.2 Cytograms

The Volume/Hemoglobin Concentration cytogram, which records the two light-scatter measurements of the sample (high-angle light scatter and low-angle light scatter), are featured in Figure 4.10 for the final time step (10,000 s) in each flow regime. Each of the Low Flow regimes (with and without the stainless steel mesh) have most of the RBC's hemoglobin concentration bound between 28 and 41 g/dL. In addition, the majority of the RBC's have a mean volume between 60 and 120 fL. Some of the RBCs begin to drift outside the normal range of volume and hemoglobin concentration in the last time step of each Low Flow experiment,

Figure 4.6. In contrast, the High Flow experiments show very little RBC presence during the last time step of the experiment, Figure 4.7. During the previous time steps, the RBC concentration stays remarkably well-bound by the volume and hemoglobin concentration limits.

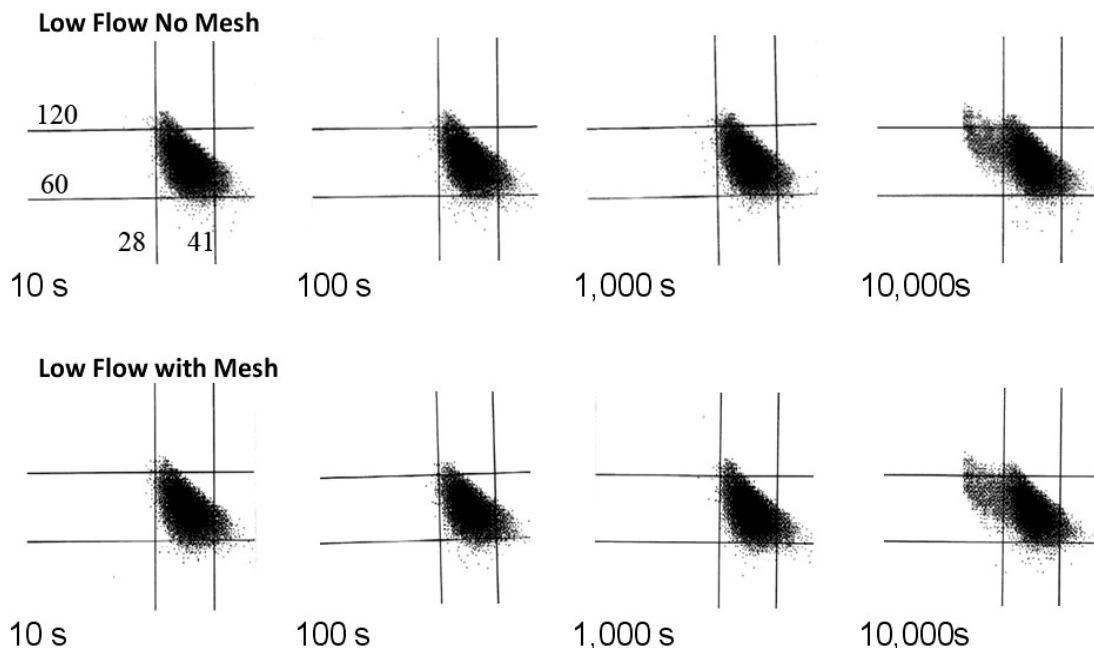


Figure 4.6. Cytograms for the Low Flow regime are pictured above at four time points: 10s, 100s, 1,000s and 10,000s. The composition of the sample remains largely unchanged, except for the last time point (10,000s) when some of the cells are detected outside the normal RBC volume and hemoglobin concentration.

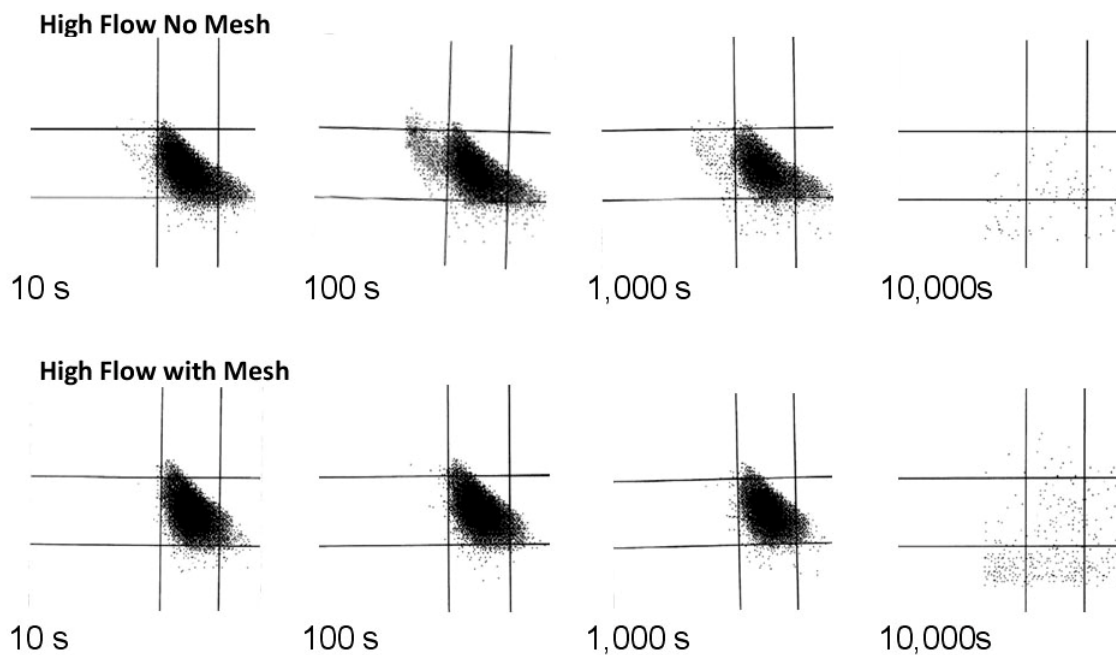


Figure 4.7. Cytograms for the High Flow regime are pictured above at four time points: 10s, 100s, 1,000s and 10,000s. The samples undergo the most drastic change at the last time point, where almost no RBCs fall within the normal range of volume and hemoglobin concentration per cell.

4.4.3 Light Microscopy Characterization

All flow regimes were also analyzed under a light microscope at a magnification of 400x to characterize the RBC changes during each of the experiments. As is the case with the cytograms, little change happens in both of the Low Flow regimes over the prescribed time period.

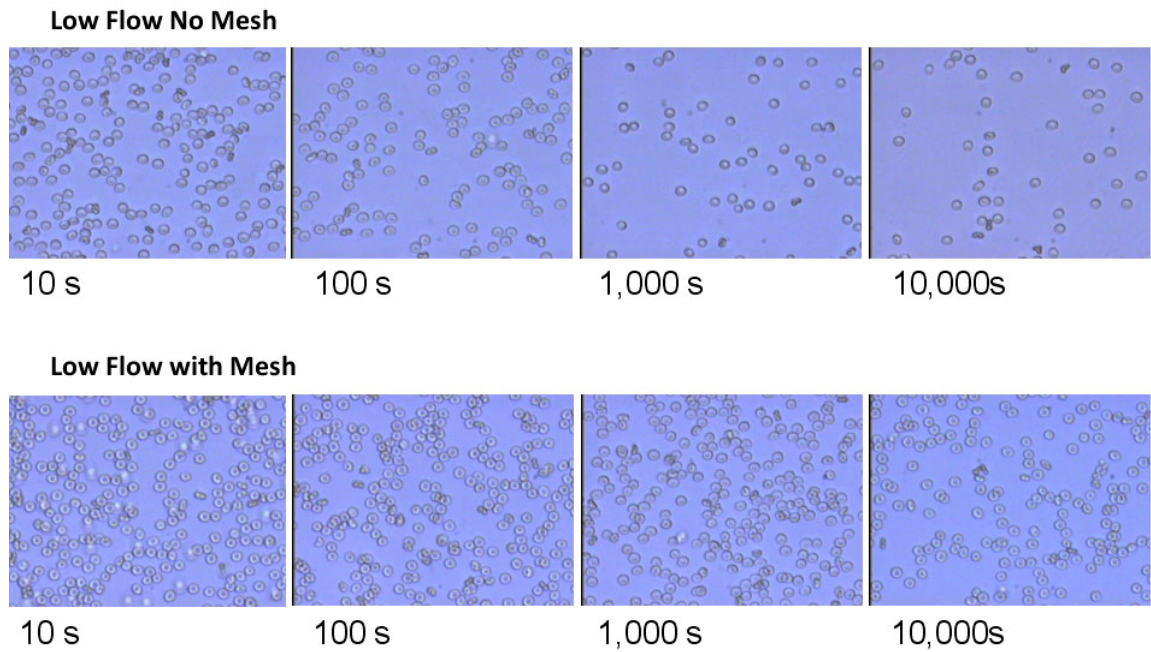


Figure 4.8. Samples from the Low Flow regime are seen at four different time points in the experiment.

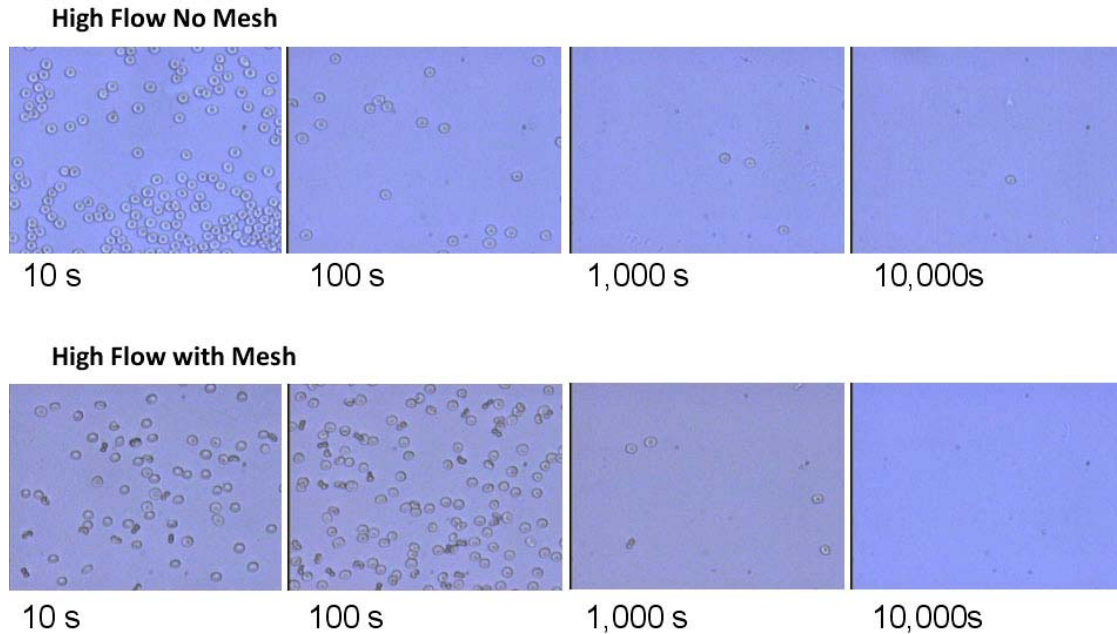


Figure 4.9 Samples from the High Flow regime are seen at four different time points in the experiment.

4.5 Discussion

4.5.1 Red Blood Cells

The RBC concentration in each of the two High Flow experiments continually decreased with time, indicating that the high level of shear induced by this flow rate caused the RBCs to fracture. The Low Flow experiments, on the other hand, did not experience a noticeable change in the RBC concentration over time, demonstrating that the low level of shear created by this flow is not enough to cause hemolysis, even under prolonged exposure. The idea of a threshold for hemolysis is discussed further by Yeleswarapu, et. al. [52]. The presence of the stainless steel mesh did not have an impact on this measurement in either the High Flow or the Low Flow regime.

4.5.2 RBC Fragment Detection

A surprising finding in this study was the increased volume of RBC fragments detected during the two flow experiments using the High Flow regime. When the stainless steel mesh is present, the number of these fragments is considerable higher (8.96×10^5 cells/ μL) during the last time point than when no mesh (2.69×10^5 cells/ μL) is inserted. This indicates that the presence of the mesh has some impact on RBC hemolysis. However, the overall effect is minimal since the mesh does not effect the total RBC concentration.

The cytograms of Figure 4.10 and Figure 4.11 provide a direct illustration of the impact shear-based hemolysis has on the RBC population in a given sample after prolonged exposure. Most normal RBC's have a cell volume of 60-120 fL and a hemoglobin concentration of 28-41 g/dL. For the High Flow regime, the RBC count drops significantly while the Low Flow regime retains most of its RBC's within the normal range.

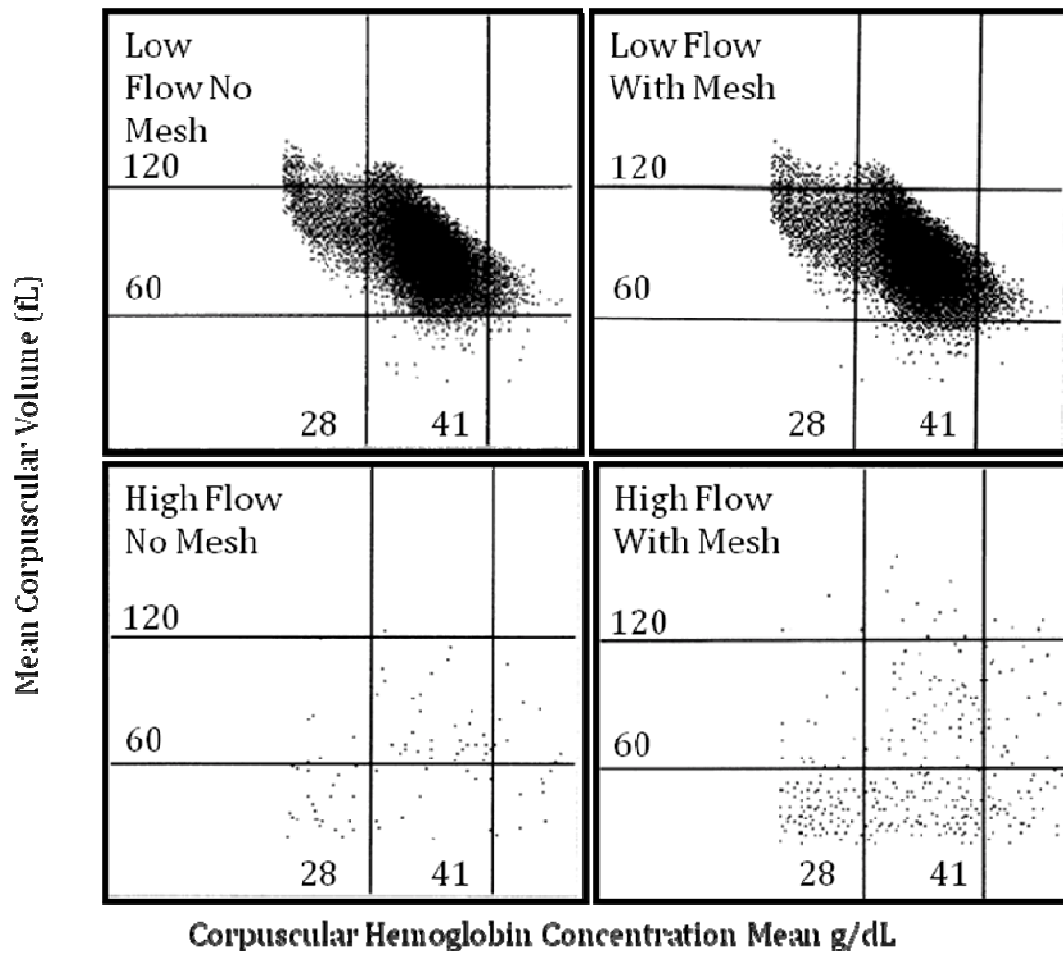


Figure 4.10. The Volume/Hemoglobin Concentration cytogram is captured above for the four flow experiments at the final time point (10,000 seconds). The hemoglobin concentration is plotted along the x-axis and the volume is plotted along the y-axis. For normal RBC's, the majority of cells should fall in the central square.

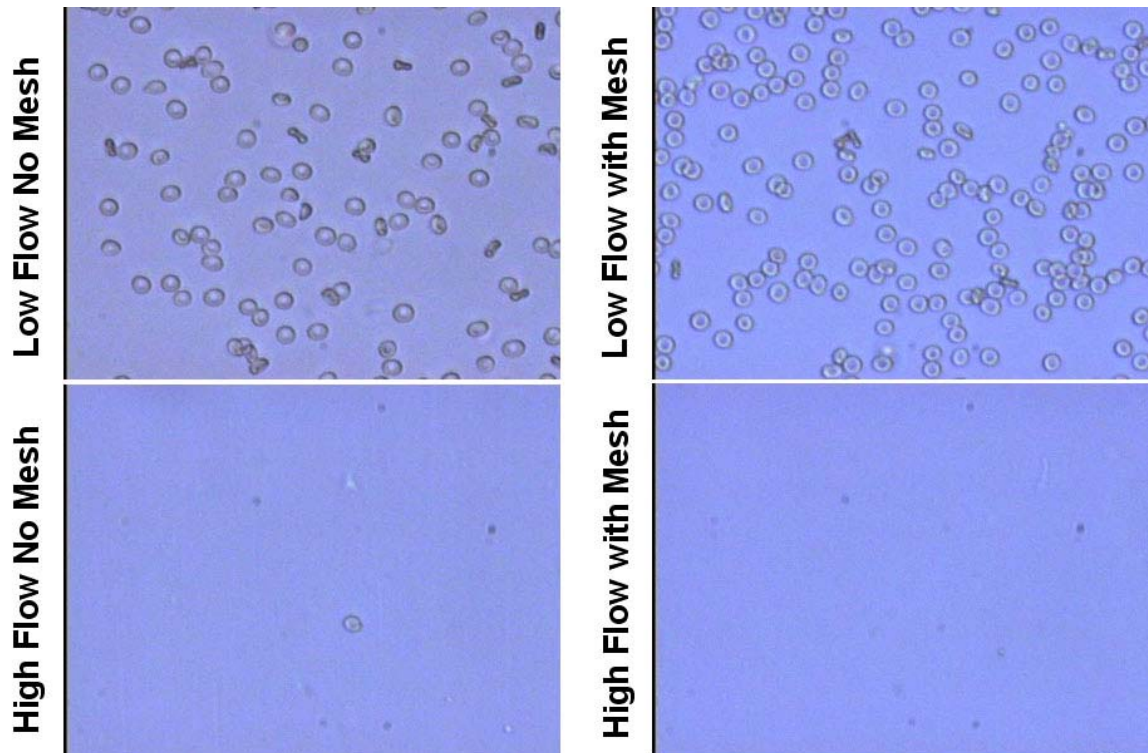


Figure 4.11. Light microscope image of RBCs during the last time point of all four flow regimes (Low Flow No Mesh, Low Flow Mesh, High Flow No Mesh, High Flow Mesh) examined in this study.

4.5.3 Conclusion

Low Flow regimes experience little damage to RBC's suggesting that it is safe to partially obstruct flow to the renal arteries. When higher flows are seen, there is significant blood damage to the RBC's. Unless there is drastic change to the flow conditions in this part of the anatomy, device placement should now cause damage to the RBCs.

4.5.4 Future Work

Further exploration into how different mesh geometries affect RBC's fragmentation is an important aspect, as it would influence design of future implantable devices and

deployment of existing devices in difficult anatomies. Various mesh designs (strut geometry, thickness and width) and mesh materials, not just stainless steel, including the influence of surface finish and coatings should also be explored. In addition, an augmented model of hemolysis should be created to incorporate the creation of RBC fragments detected in this work. Experiments in circulatory (animal shunt) models are worth conducting to understand these effects under more clinically relevant conditions.

References

1. Prisant, L.M. and J.S. Mondy, 2004, "Abdominal Aortic Aneurysm," *The Journal of Clinical Hypertension*, **6**(2), p. 85-89.
2. Gillum, R.F., 1995, "Epidemiology of aortic aneurysm in the United States," *Journal of Clinical Epidemiology*, **48**(11), p. 1289-1298.
3. Jayr, C., et al., 1993, "Preoperative and intraoperative factors associated with prolonged mechanical ventilation. A study in patients following major abdominal vascular surgery," *Chest*, **103**(4), p. 1231-1236.
4. Sakalihan, N., et al., 1996, "Activated forms of MMP2 and MMP9 in abdominal aortic aneurysms," *Journal of vascular surgery : official publication, the Society for Vascular Surgery [and] International Society for Cardiovascular Surgery, North American Chapter*, **24**(1), p. 127-133.
5. Reed, W.W., et al., 1997, "Learning From the Last Ultrasound: A Population-Based Study of Patients With Abdominal Aortic Aneurysm," *Arch Intern Med*, **157**(18), p. 2064-2068.
6. Delin, et al., *Growth rate of abdominal aortic aneurysms as measured by computed tomography*. Vol. 72. 1985, Chichester, ROYAUME-UNI: Wiley.
7. Shah, P.K., 1997, "Inflammation, Metalloproteinases, and Increased Proteolysis : An Emerging Pathophysiological Paradigm in Aortic Aneurysm," *Circulation*, **96**(7), p. 2115-2117.
8. Herron, G.S., et al., 1991, "Connective tissue proteinases and inhibitors in abdominal aortic aneurysms. Involvement of the vasa vasorum in the pathogenesis of aortic aneurysms," *Arteriosclerosis, Thrombosis, and Vascular Biology*, **11**(6), p. 1667-1677.
9. Holmes, D.R., et al., 1995, "Medial neovascularization in abdominal aortic aneurysms: A histopathologic marker of aneurysmal degeneration with pathophysiologic implications," *Journal of Vascular Surgery*, **21**(5), p. 761-772.
10. MacSweeney, S.T.R., J.T. Powell, and R.M. Greenhalgh, 1994, "Pathogenesis of abdominal aortic aneurysm," *British Journal of Surgery*, **81**(7), p. 935-941.
11. Vardulaki, K.A., et al., 2000, "Quantifying the risks of hypertension, age, sex and smoking in patients with abdominal aortic aneurysm," *British Journal of Surgery*, **87**(2), p. 195-200.
12. Brown, L.C., J.T. Powell, and U.K.S.A.T.P.w. The, 1999, "Risk Factors for Aneurysm Rupture in Patients Kept Under Ultrasound Surveillance," *Annals of Surgery*, **230**(3), p. 289.
13. Kuivaniemi, H., et al., 2003, "Familial abdominal aortic aneurysms: Collection of 233 multiplex families," *Journal of Vascular Surgery*, **37**(2), p. 340-345.
14. Pleumeekers, H.J.C.M., et al., 1995, "Aneurysms of the Abdominal Aorta in Older Adults," *American Journal of Epidemiology*, **142**(12), p. 1291-1299.
15. Scott, R.A.P., et al., 1995, "Influence of screening on the incidence of ruptured abdominal aortic aneurysm: 5-year results of a randomized controlled study," *British Journal of Surgery*, **82**(8), p. 1066-1070.

16. Castleden, W.M., J.C. Mercer, and S. The Members of the West Australian Vascular, 1985, "Abdominal aortic aneurysms in Western Australia: Descriptive epidemiology and patterns of rupture," *British Journal of Surgery*, **72**(2), p. 109-112.
17. McFarlane, M.J., 1991, "The Epidemiologic Necropsy for Abdominal Aortic Aneurysm," *JAMA: The Journal of the American Medical Association*, **265**(16), p. 2085-2088.
18. Bengtsson, et al., *Increasing prevalence of abdominal aortic aneurysms : a necropsy study*. Vol. 158. 1992.
19. Lederle, F.A., et al., 1997, "Prevalence and Associations of Abdominal Aortic Aneurysm Detected through Screening," *Annals of Internal Medicine*, **126**(6), p. 441-449.
20. Szilagyi, D.E., J.P. Elliott, and R.F. Smith, 1972, "Clinical Fate of the Patient With Asymptomatic Abdominal Aortic Aneurysm and Unfit for Surgical Treatment," *AMA Arch Surg*, **104**(4), p. 600-606.
21. Conway, K.P., et al., 2001, "Prognosis of patients turned down for conventional abdominal aortic aneurysm repair in the endovascular and sonographic era: Szilagyi revisited?," *Journal of Vascular Surgery*, **33**(4), p. 752-757.
22. Cronenwett, et al., *Actuarial analysis of variables associated with rupture of small abdominal aortic aneurysms*. Vol. 98. 1985, New York, NY, ETATS-UNIS: Elsevier.
23. Nicholls, S.C., et al., 1998, "Rupture in small abdominal aortic aneurysms," *Journal of Vascular Surgery*, **28**(5), p. 884-888.
24. 1998, "Mortality results for randomised controlled trial of early elective surgery or ultrasonographic surveillance for small abdominal aortic aneurysms," *The Lancet*, **352**(9141), p. 1649-1655.
25. Cruz, C.P., et al., 2001, "Abdominal Aortic Aneurysm Repair," *Vascular and Endovascular Surgery*, **35**(5), p. 335-344.
26. Parodi, J.C., J.C. Palmaz, and H.D. Barone, 1991, "Transfemoral Intraluminal Graft Implantation for Abdominal Aortic Aneurysms," *Annals of Vascular Surgery*, **5**(6), p. 491-499.
27. Matsumura, J.S., et al., 2003, "A multicenter controlled clinical trial of open versus endovascular treatment of abdominal aortic aneurysm," *Journal of Vascular Surgery*, **37**(2), p. 262-271.
28. Kamineni, R. and R.R. Heuser, 2004, "Abdominal Aortic Aneurysm," *Journal of Interventional Cardiology*, **17**(6), p. 437-445.
29. Hobo, R. and J. Buth, 2006, "Secondary interventions following endovascular abdominal aortic aneurysm repair using current endografts. A EUROSTAR report," *Journal of Vascular Surgery*, **43**(5), p. 896-896.
30. Howell, B.A., et al., 2007, "Computational Fluid Dynamics Within Bifurcated Abdominal Aortic Stent-Grafts," *Journal of Endovascular Therapy*, **14**(2), p. 138-143.
31. Carpenter, J.P., et al., 2001, "Impact of exclusion criteria on patient selection for endovascular abdominal aortic aneurysm repair," *Journal of Vascular Surgery*, **34**(6), p. 1050-1054.

32. Rayz, V.L., et al., 2008, "Numerical Modeling of the Flow in Intracranial Aneurysms: Prediction of Regions Prone to Thrombus Formation," *Annals of Biomedical Engineering*, **36**(11), p. 1793-1804.
33. Zarins, C.K. and C.A. Taylor, 2009, "Endovascular Device Design in the Future: Transformation From Trial and Error to Computational Design," *Journal of Endovascular Therapy*, **16**(SupplementI), p. I-12-I-21.
34. Brooks, A.N. and T.J.R. Hughes, 1982, "Streamline upwind/Petrov-Galerkin formulations for convection dominated flows with particular emphasis on the incompressible Navier-Stokes equations," *Computer Methods in Applied Mechanics and Engineering*, **32**(1-3), p. 199-259.
35. Jordan, et al., *Abdominal aortic aneurysms in high-risk surgical patients: Comparison of open and endovascular repair. Discussion*. 2003, Hagerstown, MD, ETATS-UNIS: Lippincott Williams & Wilkins. 8.
36. Vallabhaneni, S.R. and P.L. Harris, 2001, "Lessons learnt from the EUROSTAR registry on endovascular repair of abdominal aortic aneurysm repair," *European Journal of Radiology*, **39**(1), p. 34-41.
37. Harris, P.L., et al., 2000, "Incidence and risk factors of late rupture, conversion, and death after endovascular repair of infrarenal aortic aneurysms: The EUROSTAR experience," *Journal of Vascular Surgery*, **32**(4), p. 739-749.
38. Schurink, G.W.H., N.J.M. Aarts, and J.H. van Bockel, 1999, "Endoleak after stent-graft treatment of abdominal aortic aneurysm: a meta-analysis of clinical studies," *British Journal of Surgery*, **86**(5), p. 581-587.
39. Kim, H.J., et al., 2009, "Augmented Lagrangian method for constraining the shape of velocity profiles at outlet boundaries for three-dimensional finite element simulations of blood flow," *Computer Methods in Applied Mechanics and Engineering*, **198**(45-46), p. 3551-3566.
40. Yushkevich, P.A., et al., 2006, "User-guided 3D active contour segmentation of anatomical structures: Significantly improved efficiency and reliability," *NeuroImage*, **31**(3), p. 1116-1128.
41. Wang, K.C., R.W. Dutton, and C.A. Taylor, 1999, "Improving geometric model construction for blood flow modeling," *Engineering in Medicine and Biology Magazine, IEEE*, **18**(6), p. 33-39.
42. Niessen, W., et al., *A Software Framework for Creating Patient Specific Geometric Models from Medical Imaging Data for Simulation Based Medical Planning of Vascular Surgery*, in *Medical Image Computing and Computer-Assisted Intervention – MICCAI 2001*. 2001, Springer Berlin / Heidelberg. p. 449-456.
43. Xiong, G., "Simulation of blood flow in deformable vessels using subject-specific geometry and assigned variable mechanical wall properties," *International journal for numerical methods in biomedical engineering*.
44. Xiong, G., G. Choi, and C.A. Taylor, "Virtual interventions for image-based blood flow computation," *Computer-Aided Design*, **In Press, Corrected Proof**.
45. O'Kelly, T.J. and B.P. Heather, 1989, "General practice-based population screening for abdominal aortic aneurysms: A pilot study," *British Journal of Surgery*, **76**(5), p. 479-480.

46. Molony, D.S., et al., 2008, "Geometrical Enhancements for Abdominal Aortic Stent-Grafts," *Journal of Endovascular Therapy*, **15**(5), p. 518-529.
47. Wever, J.J., et al., 2000, "Dilatation of the Proximal Neck of Infrarenal Aortic Aneurysms after Endovascular AAA Repair," *European Journal of Vascular and Endovascular Surgery*, **19**(2), p. 197-201.
48. 1988, "More on Simplified Calculation of Body-Surface Area," *New England Journal of Medicine*, **318**(17), p. 1130-1130.
49. Toy, S.M., J. Melbin, and A. Noordergraaf, 1985, "Reduced Models of Arterial Systems," *Biomedical Engineering, IEEE Transactions on*, **BME-32**(2), p. 174-176.
50. Bludszweit, C., 1995, "Model for a General Mechanical Blood Damage Prediction," *Artificial Organs*, **19**(7), p. 583-589.
51. Garon, A. and M.-I. Farinas, 2004, "Fast Three-dimensional Numerical Hemolysis Approximation," *Artificial Organs*, **28**(11), p. 1016-1025.
52. Yeleswarapu, K.K., et al., 1995, "A Mathematical Model for Shear-Induced Hemolysis," *Artificial Organs*, **19**(7), p. 576-582.
53. Arora, D., M. Behr, and M. Pasquali, 2004, "A Tensor-based Measure for Estimating Blood Damage," *Artificial Organs*, **28**(11), p. 1002-1015.
54. Bluestein, M. and L. Mockros, 1969, "Hemolytic effects of energy dissipation in flowing blood," *Medical and Biological Engineering and Computing*, **7**(1), p. 1-16.
55. Giersiepen, M., et al., 1990, "Estimation of shear stress-related blood damage in heart valve prostheses--in vitro comparison of 25 aortic valves," *The International journal of artificial organs*, **13**(5), p. 300-6.
56. Bax, L., et al., 2005, "Renal Blood Flow Measurements with Use of Phase-Contrast Magnetic Resonance Imaging: Normal Values and Reproducibility," *Journal of Vascular and Interventional Radiology*, **16**(6), p. 807-814.
57. Nosé, Y., 1998, "Design and Development Strategy for the Rotary Blood Pump," *Artificial Organs*, **22**(6), p. 438-446.
58. Desgranges, P., et al., 1997, "Aortic Stents Covering the Renal Arteries Ostia: An Animal Study," *Journal of Vascular and Interventional Radiology*, **8**(1, Part 1), p. 77-82.
59. Birch, P.C., et al., 1999, "The Effects of Crossing Porcine Renal Artery Ostia with Various Endovascular Stents," *European Journal of Vascular and Endovascular Surgery*, **17**(3), p. 185-190.
60. Leverett, L.B., et al., 1972, "Red Blood Cell Damage by Shear Stress," *Biophysical Journal*, **12**(3), p. 257-273.
61. Nobili, M., et al., *Platelet Activation Due to Hemodynamic Shear Stresses: Damage Accumulation Model and Comparison to In Vitro Measurements. [Miscellaneous Article]*. 2008: *ASAIO Journal* January/February 2008;54(1):64-72.
62. Purves, W.K.D.S., Gordon H. Orians, H. Craig Heller, *Life: The Science of Biology*. 7 ed. 2004, Sunderland: Sinauer Associates.
63. Fu, Q. and W. Sun, 2001, "Mie Theory for Light Scattering by a Spherical Particle in an Absorbing Medium," *Appl. Opt.*, **40**(9), p. 1354-1361.